The Impact of Airborne Radio Occultation Observations on the Simulation of Hurricane Karl (2010)

X. M. CHEN,[a] S.-H. CHEN,[a] J. S. HAASE,[b] B. J. MURPHY,[c,d] K.-N. WANG,[e] J. L. GARRISON,[c] S. Y. CHEN,[f] C. Y. HUANG,[g] L. ADHIKARI,[h] AND F. XIE[h]

[a] *University of California, Davis, Davis, California*
[b] *Scripps Institution of Oceanography, University of California, San Diego, La Jolla, California*
[c] *Purdue University, West Lafayette, Indiana*
[d] *Edison State Community College, Piqua, Ohio*
[e] *Jet Propulsion Laboratory, California Institute of Technology, Pasadena, California*
[f] *GPS Science and Application Research Center (GPSARC), National Central University, Taoyuan, Taiwan*
[g] *Department of Atmospheric Sciences, National Central University, Taoyuan, Taiwan*
[h] *Texas A&M University–Corpus Christi, Corpus Christi, Texas*

(Manuscript received 2 January 2017, in final form 8 October 2017)

ABSTRACT

This study evaluates, for the first time, the impact of airborne global positioning system radio occultation (ARO) observations on a hurricane forecast. A case study was conducted of Hurricane Karl during the Pre-Depression Investigation of Cloud-Systems in the Tropics (PREDICT) field campaign in 2010. The assimilation of ARO data was developed for the three-dimensional variational (3DVAR) analysis system of the Weather Research and Forecasting (WRF) Model version 3.2. The impact of ARO data on Karl forecasts was evaluated through data assimilation (DA) experiments of local refractivity and nonlocal excess phase (EPH), in which the latter accounts for the integrated horizontal sampling along the signal ray path. The tangent point positions (closest point of an RO ray path to Earth's surface) drift horizontally, and the drifting distance of ARO data is about 2 to 3 times that of spaceborne RO, which was taken into account in these simulations.

Results indicate that in the absence of other satellite observations, the assimilation of ARO EPH resulted in a larger impact on the analysis than local refractivity did. In particular, the assimilation of ARO observations at the actual tangent point locations resulted in more accurate forecasts of the rapid intensification of the storm. Among all experiments, the best forecast was obtained by assimilating ARO data with the most accurate geometric representation, that is, the use of nonlocal EPH operators with tangent point drift, which reduced the error in the storm's predicted minimum sea level pressure (SLP) by 43% beyond that of the control experiment.

1. Introduction

The prediction of tropical cyclones is important because of its great impacts on safety and on preventing property damage and economic losses (Willoughby et al. 2007; Willoughby 2012). Prediction remains a challenging task because of the lack of understanding of how individual hurricanes form and because too few finescale measurements are available over storm regions to help advance our knowledge. Early studies identified a set of necessary conditions for tropical cyclone genesis based on global observations and climatology (e.g., Riehl 1954; Gray 1968, 1998): warm water temperature within the surface mixed layer, initial cyclonic relative vorticity, moist midtroposphere, weak vertical wind shear, and the presence of the Coriolis force. Various combinations and mathematical formulations of these conditions were used to develop prediction parameters (e.g., Gray 1979; DeMaria et al. 2001; Emanuel and Nolan 2004; Camargo et al. 2007; Bruyère et al. 2012), which suggested some predictability of tropical cyclone activity on the year-to-year and seasonal scales. Nevertheless, these studies also pointed out that the climatological parameters are not sufficient to explain the development of individual tropical cyclones.

Both obtaining a better understanding of tropical cyclogenesis and achieving more accurate numerical

Corresponding author: Dr. Shu-Hua Chen, shachen@ucdavis.edu

DOI: 10.1175/MWR-D-17-0001.1

model forecasts of tropical cyclone evolution depend heavily on available observations and their quality. Observations can help reduce the errors in model initial conditions through data assimilation (DA). Satellite observations are particularly important for tropical cyclone forecasting over the ocean, where in situ surface and upper-air observations are sparse. For example, case studies have shown that temperature and moisture retrievals from infrared and near-infrared sounders, such as the Moderate Resolution Imaging Spectroradiometer (MODIS), (Chen et al. 2008; Liu et al. 2011), Atmospheric Infrared Sounder (AIRS), and Infrared Atmospheric Sounding Interferometer (ASI) (Reale et al. 2009; Li and Liu 2009; Liu and Li 2010), improved hurricane track and intensity forecasts. Other case studies have shown that the direct assimilation of satellite radiance has a positive impact on tropical cyclone predictions as well (e.g., Z. Liu et al. 2012; Schwartz et al. 2012; Newman et al. 2015; Routray et al. 2016; Choi et al. 2017). However, satellite observations are usually either relatively coarse in vertical resolution or affected by clouds and heavy rainfall. Therefore, their impact on hurricane prediction is usually limited to the large-scale environment. In contrast to global satellite products, near-storm airborne observations provide direct measurements of the environment in the vicinity of the storms at a high resolution (e.g., Weissmann et al. 2011; Aberson et al. 2015). These have made important contributions to storm forecasting, and recently, methods for operational assimilation of reconnaissance data, such as Doppler vector winds, have been developed (Aksoy et al. 2012; Weng and Zhang 2012; Zhang and Weng 2015). This potential for exploiting aircraft data in an operational setting partially motivates the present study on airborne radio occultation (ARO). Before introducing ARO data, we first review some of the advances that might be expected, based on recent data assimilation studies using spaceborne global positioning system radio occultation (SRO).

Radio occultation (RO) measurements (spaceborne and airborne) are mostly insensitive to clouds and rainfall, a particularly useful feature when studying severe weather systems, and they sample the atmosphere at very high vertical resolution, compared to conventional passive satellite observations (Yunck et al. 1988; Ware et al. 1996; Kursinski et al. 1996, 1997). Many assimilation studies showed a positive impact of SRO measurements on global weather forecasts, especially where other observations are scarce, and in the upper troposphere to lower stratosphere, where RO data quality is typically the best (e.g., Zou et al. 2004; Healy et al. 2005; Healy and Thépaut 2006; Cucurull and Derber 2008; Cucurull 2010). Studies using simulated observations have further suggested that as more RO data are assimilated, their impact continues to improve (e.g., Harnisch et al. 2013; Bauer et al. 2014; Leidner et al. 2017). The impact of SRO observations has been assessed in operational centers such as the European Centre for Medium-Range Weather Forecasts (ECMWF) (Dee et al. 2011; Cardinali and Healy 2014), the National Centers for Environmental Prediction (NCEP) (Cucurull et al. 2007; Cucurull 2010), Météo-France (Poli et al. 2009), the Met Office (Healy et al. 2005; Buontempo et al. 2008; Rennie 2010), the German Meteorological Office (Anlauf et al. 2011), the Australian Bureau of Meteorology (Le Marshall et al. 2012), and others. As a result, SRO missions that were once proof of concept have evolved into operational systems with low latency of data due to their statistically demonstrated impact in the upper troposphere to lower stratosphere (Bauer et al. 2014; Cardinali and Healy 2014).

For individual storms on the regional scale, it is more difficult to statistically assess the impact or value of an individual observation type of coarse horizontal resolution such as SRO. However, the assimilation of SRO data can sometimes still show a positive impact in individual case studies. For example, the assimilation of SRO observations can improve predictions of tropical cyclone intensity (e.g., Kunii et al. 2012), rainfall (e.g., Huang et al. 2005; Chen et al. 2009), and track (e.g., Kueh et al. 2009) through adjustments of the temperature and moisture fields. H. Liu et al. (2012) reached similar conclusions for Hurricane Ernesto (2006) and further emphasized the importance of SRO observations in the lower troposphere below 6 km. In the first study that attempts to synthesize the impact of SRO on the forecast of a large dataset of tropical cyclones, Chen et al. (2015) showed that the assimilation of SRO observations produced a statistically significant improvement in 11 out of 31 typhoon track forecasts between 2008 and 2010.

While sharing most of the advantages of SRO, ARO can densely sample a targeted area in a manner complementary to dropsondes, which is crucial for a regional study of the highly variable tropical cyclone environment. This study aims to provide an initial estimate of the potential value of ARO observations by investigating their impact on the prediction of Hurricane Karl in 2010. The ARO observations were taken from the National Science Foundation Gulfstream-V (G-V) aircraft during the Pre-Depression Investigation of Cloud-Systems in the Tropics (PREDICT) field campaign in 2010 (Evans et al. 2012; Montgomery et al. 2012), along with dropsondes and microphysical measurements during the pregenesis stage of several tropical storms. ARO data are complementary to dropsonde measurements deployed along the paths of reconnaissance flights because their tangent points, that is, the closest points of the RO ray paths to the earth's

surface, drift sideways, away from or toward the flight path, as the transmitting satellite moves with respect to the receiver. As a result of this, as well as the long horizontal integration over the ray path, a larger area is sampled by the ARO observations, compared to dropsondes.

Radioholographic retrieval methods, that is, phase matching (PM) (Wang et al. 2017; Jensen et al. 2004) and full spectrum inversion (Adhikari et al. 2016; Jensen et al. 2003), have been successfully implemented for ARO measurements to retrieve the refractive bending angle reliably in the presence of atmospheric multipath and to eliminate errors in the geometric optics bending angle retrievals . From the bending angles, refractivity profiles can be retrieved using the Abel inversion for a receiver inside the atmosphere, a procedure explained in detail in Healy et al. (2002), Muradyan et al. (2011), and Xie et al. (2008). In the neutral atmosphere, the relationship between refractivity (N) at L-band radio frequencies and model variables was formulated by Smith and Weintraub (1953) and reviewed by many studies (e.g., Rüeger 2002; Aparicio and Laroche 2011; Cucurull 2010; Healy 2011). The most commonly used form of the relationship is the following:

$$N = (n-1)\times 10^6 = 77.6\frac{P}{T} + 3.73\times 10^5\frac{e}{T^2}, \qquad (1)$$

where n is the refractive index, e is water vapor pressure (hPa), P is total air pressure (hPa), and T is temperature (K). The quantity N is retrieved as a function of geometric height (e.g., Kursinski et al. 1997; Hajj et al. 2002; Kuo et al. 2004). The goal of this study is to present an assessment of the impact of assimilating these ARO refractivity profiles on the prediction of Hurricane Karl's development in 2010.

While it is relatively straightforward to assimilate vertical profile values of RO local refractivity, the assigned observational errors need to carefully take into account the assumption of local spherical symmetry of the atmosphere in the proximity of the ray paths, as well as instrumental and representativeness errors. Xie et al. (2008) investigated different error sources that affect data quality of local ARO measurements in the case of a frontal system. They found that the assumption of spherical symmetry is the largest source of error in RO data retrievals for this case, with up to 4.5% in refractivity under worst-case conditions when there are large horizontal density gradients along the rays. On the other hand, when nonlocal pseudo-observations of excess phase (EPH) (i.e., path-integrated refractivity) are used, the assigned observational error can be reduced (Sokolovskiy 2005a,b). In this study, the impact of ARO data on Karl forecasts using both the local and nonlocal operators will be evaluated and compared.

The paper is organized as follows. Section 2 details the newly developed numerical tools, the numerical experiment design, and the data used. Section 3 examines the impact of the more conventional reconnaissance dropsonde dataset on Karl forecasts before examining ARO. The impact of the ARO observations on key variables of the analysis is then presented in section 4, and the consequent impact on the forecast is presented in section 5. The summary and discussion of the main conclusions are presented in section 6.

2. Numerical tools and experiment design

The numerical tools used in this study include a forecasting system and a data assimilation system. The Weather Research and Forecasting (WRF) Model version 3.2 (Skamarock et al. 2008) is used for numerical forecasts. Because of the limitation of computational resources, a three-dimensional variational (3DVAR) method, instead of an ensemble Kalman filter (e.g., H. Liu et al. (2012); Leidner et al. 2017) or a hybrid method (e.g., Schwartz et al. 2013; Wang 2011), is used to assimilate observations. The WRF 3DVAR data assimilation system (Barker et al. 2004; Huang et al. 2009; Barker et al. 2012) is chosen as our analysis tool. Before the experimental design is introduced, Hurricane Karl, the ARO data, the EPH operator, and ARO observational errors are briefly summarized.

a. *Hurricane Karl*

As described in the National Hurricane Center (NHC) tropical storm report (Stewart 2011), the pre-Karl system originated from a westward-propagating wave that merged with an upper-level trough on 8 September 2010. Karl's early period of development was characterized by bursts of convection that were regulated by the diurnal radiation cycle (Melhauser and Zhang 2014). Misaligned surface-to-midlevel vortices were observed until 13 September (Davis and Ahijevych 2012), which may be one reason why storm development was delayed.

Karl reached tropical storm strength (i.e., genesis) at around 1800 UTC 14 September 2010 before crossing the Yucatan Peninsula. When crossing the peninsula, the storm continued on a westward track under the forcing of a subtropical ridge to its north. The storm's surface low weakened due to surface friction and a loss of contact with the warm sea surface, while the midlevel vortex strengthened, and the cyclone gained a better vertical alignment (Stewart 2011; Davis and Ahijevych 2012). Rapid intensification (RI) occurred soon after the storm entered the Gulf of Mexico, and it became a category 3 hurricane on 17 September. The hurricane weakened later that day, likely due to stronger vertical

wind shear and entrainment of dry downsloping air from the Sierra Madre in Mexico. Final landfall occurred over the coast of Mexico at 1645 UTC 17 September, bringing heavy rainfall, flooding, and mudslides (Stewart 2011).

b. *The airborne radio occultation measurements from PREDICT*

A total of six missions were deployed to measure the pregenesis environment of Karl during the 5 days prior to genesis (10–14 September). For the purpose of this study, 10 profiles from the second-to-last flight within the 3-h time period centered at 1200 UTC 13 September were assimilated.

Two observational operators for assimilation of ARO measurements were evaluated: local refractivity and nonlocal pseudo-EPH, in which the latter is the integration of the local refractivity measurements along hypothetical straight ray paths (Sokolovskiy et al. 2005a,b). The local refractivity observational operator has been more commonly used and described than the excess phase operator has (e.g., Cucurull et al. 2007), so the latter is briefly introduced in the next section.

c. *The ARO excess phase operator*

The nonlocal EPH operator accounts for the highly heterogeneous environment of a developing hurricane. The EPH operator in the WRF DA system implemented by Chen et al. (2009) for SRO measurements was used. The algorithm assumes a straight ray path tangent to the real ray path at the tangent point, oriented along the observed azimuth angle, to calculate the observed and background EPH (Sokolovskiy et al. 2005a, b; Syndergaard et al. 2005). The model background refractivity at every ray path segment is interpolated from neighboring grid cells to calculate the background EPH. This approach is less expensive computationally than full ray-tracing algorithms where ray path direction would change as a function of refractivity gradient. For the purpose of this study, we modified the existing SRO EPH operator to accommodate the geometry of ARO observations, where one end point of the ARO ray path is at the airplane height, which is usually below the model top. The ARO retrieval algorithm estimates a partial bending angle by removing the signal bending accumulated along the part of the ray path above the airplane, such that the retrieved refractive index is available only at heights below the airplane (Xie et al. 2008; Murphy et al. 2015). Therefore, for an airborne receiver, the integration of refractivity for both model and pseudo-observations along the predefined tangent ray path was limited to below 14 km, which was the typical cruising altitude of the G-V airplane.

d. *The ARO observational errors*

Murphy et al. (2015) showed that despite difficulties in retrieving observations near the surface, the PREDICT ARO measurements taken during the early development of Hurricane Karl were able to capture midlevel moisture variability in the developing storm environment. They estimated an accuracy of around 2% in refractivity from approximately 7 to 12 km for data from conventional receivers, and from approximately 4 to 12 km for open-loop (OL) tracking data. OL is a method of retrieving excess delay observations, even when the carrier wave cannot be tracked continuously, by using predicted Doppler shifts from a climatological model. The combined improvements in the quality of ARO retrievals from the implementation of OL tracking and PM allowed reliable retrievals down to 2 km (Wang et al. 2017). The ARO observations used in this study are OL–PM retrievals. A constant 2% uncertainty in the ARO-retrieved refractivity was estimated at all heights, based on comparisons against the nearest dropsonde measurements from all the missions during PREDICT, as well as comparisons with the ECMWF interim reanalysis (ERA-Interim) dataset (Wang et al. 2017). ARO observations below 2 km tended to produce a negative bias due to low signal-to-noise ratio (Wang et al. 2016, 2017), and thus were discarded in this study. We note that SRO observations give about 2% refractivity error at 2 km in the tropics, decreasing with height and latitude (Chen et al. 2011). In comparison, the ARO refractivity errors are larger than the spaceborne errors at upper levels near the ARO receiver altitude, where aircraft velocity errors translate to increased Doppler shift errors and, therefore, increased bending angle and refractivity errors (Xie et al. 2008; Muradyan et al. 2011; Adhikari et al. 2016).

The ARO observational errors used in DA depend on the operator used to assimilate RO observations. When assimilating local refractivity, the constant 2% was used, based on a statistical analysis of independent datasets (Murphy et al. 2015; Wang et al. 2016, 2017). When assimilating nonlocal EPH, an error of 1% in EPH, also constant with height, was used, based on the estimates in Chen et al. (2011), who found that the observational errors associated with nonlocal EPH are 1/2 to 1/3 of those of local refractivity in percentage.

e. *Numerical experiment design*

In addition to different observation operators, that is, refractivity versus excess phase, the assimilation of ARO data with drifting versus nondrifting tangent points is also examined. Errors due to neglecting the tangent point drift have been evaluated in past studies

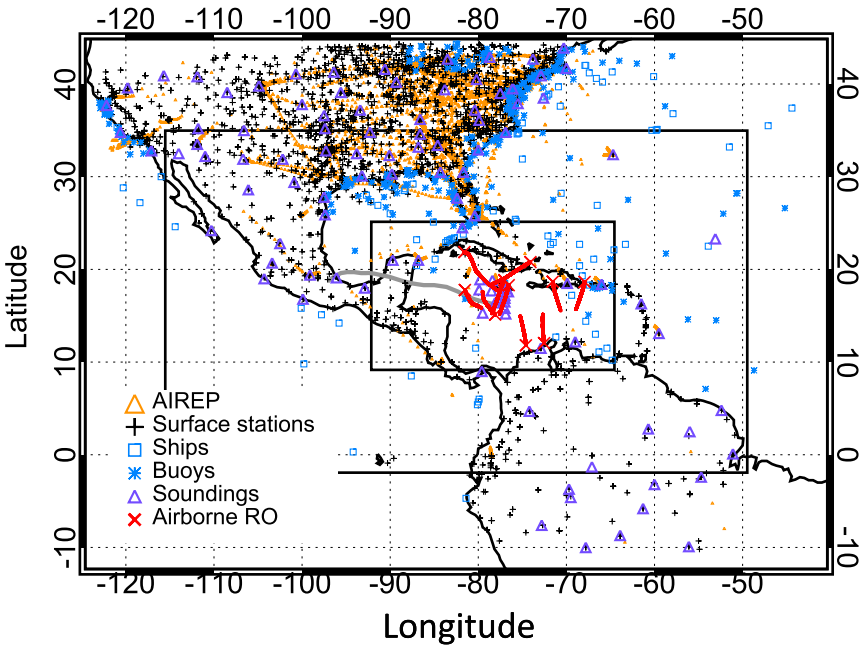

FIG. 1. The three domains used for model simulations and the assimilated observations within ±3 h of 1200 UTC 13 Sep 2010 (analysis time). The grid spacings for domains 1–3 are 27, 9, and 3 km, respectively. The nested domains are allowed to move following the vortex beyond this time. The gray line is Hurricane Karl's trajectory from the NCEP Tropical Cyclone Vitals Database.

for SRO observations (e.g., Poli and Joiner 2004; Cucurull 2012; Burrows 2015; Anlauf 2016). However, this study will further evaluate the impact of the ARO tangent point drift on Karl forecasts for the following three reasons. First, the ARO tangent point drift is very different from that of SRO, on average 2 to 3 times greater, because of the larger differential velocity between the receiver and the transmitter. Second, in contrast to SRO, where the drifting line-of-sight ray paths remain approximately in the same plane, the ARO line-of-sight ray paths are oblique to the tangent point drift. The rays sample a 3D volume of space, an effect that is exaggerated further when the tangent points drift [see Haase et al. (2014) for an illustration]. Third, because this paper describes the first attempt at assimilating ARO observations in a hurricane case study, it is both interesting and important to document the sensitivity of the numerical predictions to how the ARO observations are assimilated and what their impacts are in each case.

In this study, three datasets were used to improve model initial conditions: 1) the Global Telecommunication System (GTS) dataset, including surface observations from weather stations, ships and buoys (NOAA/NWS/NCEP/U.S. Department of Commerce 2004), upper-level aircraft in situ measurements, and radiosonde soundings (SSD/OSDPD/NESDIS/NOAA/U.S. Department of Commerce, and NOAA/NWS/NCEP/U.S. Department of Commerce 2004), 2) dropsondes released during the PREDICT field campaign; and 3) 10 ARO profiles from PREDICT taken between 1030 and 1330 UTC 13 September 2010, just prior to the cyclone reaching tropical storm status. An example of the locations of the assimilated observations is found in Fig. 1. The goal of this study is to demonstrate the potential impact of a small but high-density set of ARO observations on the prediction of Hurricane Karl. To better discern the impact of ARO observations, the satellite observations that are commonly used in operational forecast centers are excluded in this study. Because satellite data have their own uncertainties and the amount of data is huge, adding them would introduce a larger and potentially overwhelming source of uncertainty in the analysis and forecast and could obscure our evaluation of the ARO data. However, some of their large-scale impact is carried through the initial and boundary conditions provided by the global reanalysis that assimilate these satellite datasets. One should keep in mind that the impact of ARO data might be overestimated in this study due to the exclusion of these satellite observations. In the future, a statistical evaluation of assimilating ARO data on top of satellite data should be performed when ARO data become available for a larger number of cases.

Eight numerical experiments were conducted, as shown in Table 1. The control (CTRL) experiment

TABLE 1. Numerical data assimilation experiments for Hurricane Karl (2010).

Experiments	Observations assimilated
CTRL	GTS + dropsondes
GDANn	GTS + dropsondes + nondrifting ARO local refractivity
GDANd	Same as GDANn, except with drifting tangent points
GDAEn	GTS + dropsondes + nondrifting ARO excess phase
GDAEd	Same as GDAEn, except with drifting tangent points
GDAEn_no13	Same as GDAEn, but without the PRN13 ARO profile. A sensitivity test to illustrate why storm intensification was better captured in GDAEd than in GDAEn.
G	GTS only. A sensitivity test to evaluate the impact of dropsondes.
GAEd	GTS + drifting airborne RO EPH. A sensitivity test to evaluate the impact of ARO with respect to dropsondes.

assimilated GTS and dropsonde observations. It will be used to show the impact of ARO observations in the presence of conventional and dropsonde measurements. Because vertical spatial correlation between observations is neglected in the WRF DA system, the vertical resolution of the ARO profiles was reduced so that each model level contained, at most, one observation. In the case of local refractivity, the closest observation to each model height level within a column was chosen for assimilation. In the case of EPH, domain-averaged model height levels are calculated, and superobservations are computed at these average model levels using distance-weighted coefficients (Chen et al. 2009). Although the number of ARO observations when using the refractivity and excess phase operators was different, the resulting vertical distribution and number of assimilated points were very similar, around 22–23 observations per profile. The GDANn and GDANd experiments assimilated ARO local refractivity, while the GDAEn and GDAEd experiments assimilated ARO EPH. The ''n'' indicates that the tangent points of any ARO profile are vertically aligned (i.e., no drift in the horizontal), whereas the ''d'' indicates that the tangent points of any ARO profile horizontally drift as they do in reality. In both the GDANn and GDAEn experiments, the tangent points of each ARO profile were assigned to the location of the lowest one (around 2 km after quality control). This is to represent more accurately the high moisture variability at low levels. The GDAEn_no13 experiment is a sensitivity test in which a particular ARO profile (PRN13; see Fig. 2d for the location) was removed in GDAEn. The occultation PRN13 had an exceptionally long tangent point drift because an aircraft turn modified the observation geometry and extended the duration of the occultation. This profile happened to have an important impact on Hurricane Karl's forecast, depending on the assimilation strategy, which will be discussed in section 5. The last two experiments, G and GAEd, are another two sensitivity tests where dropsonde observations are not assimilated. They are designed to show the impact of dropsondes in comparison to ARO EPH (i.e., the difference between CTRL and G vs GAEd and G).

For all experiments, the WRF Model started integrating from 0000 UTC 13 September 2010, and DA was performed every 3 h from 0300 to 1200 UTC 13 September in the two outer domains. In particular, the ARO and dropsonde profiles within the 3-h time window centered at 1200 UTC 13 September 2010 were assimilated at 1200 UTC. At each time of assimilation, three outer-loop iterations were performed during the minimization of the cost function. The initial conditions at 0000 UTC 13 September and the boundary conditions of the subsequent simulation were provided by ERA-Interim. The analysis at 1200 UTC 13 September was used to initialize forecasts that ran until 0000 UTC 18 September, when the observed cyclone made landfall and dissipated. Three domains were configured for the model forecasts (Fig. 1). The horizontal grid spacings were 27, 9, and 3 km for domains 1–3, respectively, and 45 vertical levels were used, with the model top at 50 hPa. The nested domains had two-way interaction with their parent domains and moved with the cyclone during the forecast (i.e., vortex following). The same physics schemes were used for all experiments: Morrison microphysics scheme (Morrison et al. 2009), Yonsei University (YSU) planetary boundary layer scheme (Hong et al. 2006), Kain–Fritsch (KF) cumulus parameterization (Kain 2004), Rapid Radiative Transfer Model (RRTM) longwave radiation parameterization (Mlawer et al. 1997), and Goddard shortwave radiation parameterization (Chou and Suarez 1994). The cumulus parameterization was deactivated in domain 3 because convection can be reasonably resolved with a 3-km grid spacing. To have a more representative estimate of the background error covariance for this case study, we generated a height-dependent background error covariance using the National Meteorological Center (NMC) method (Parrish and Derber 1992). Sixty pairs of 12- and 24-h model forecast differences were generated

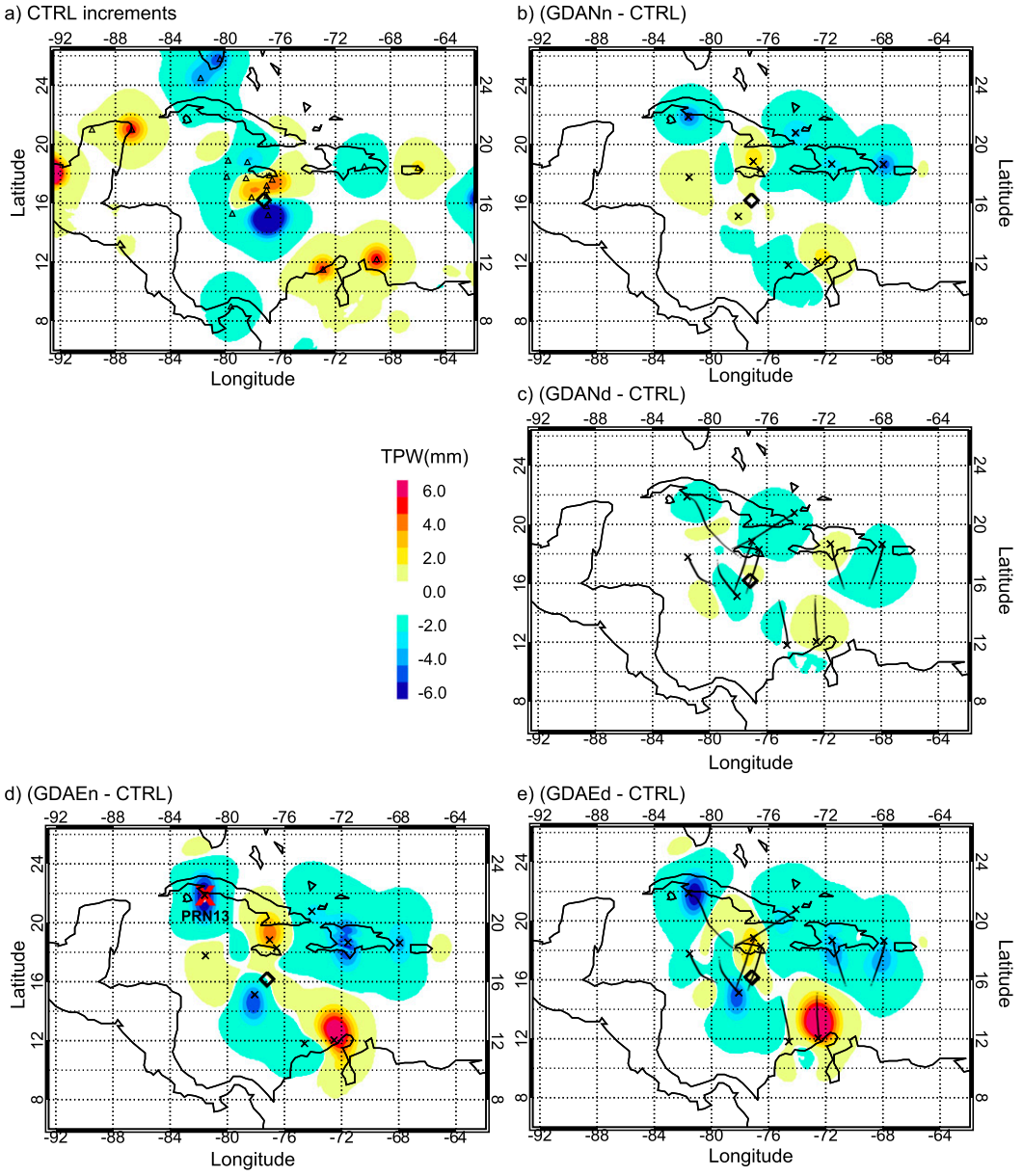

FIG. 2. (a) CTRL increments (analysis − background) of domain 2 (9 km) TPW at 1200 UTC 13 Sep. (b) CTRL TPW analysis subtracted from the GDANn TPW analysis (GDANn − CTRL) at 1200 UTC 13 Sep. (c) The (GDANd − CTRL), (d) (GDAEn − CTRL), and (e) (GDAEd − CTRL) TPWs. Triangles in (a) indicate the positions of assimilated dropsondes and radiosondes. The × symbols in (b)–(e) indicate the assimilated airborne RO tangent point positions. The red large × in (d) indicates the position of the ARO occultation profile for satellite PRN13, which was excluded in the sensitivity experiment GDAEn_no13. The black diamond indicates the estimated position of the cyclone from the NCEP Tropical Cyclone Vitals Database.

using the WRF Model, covering 1 month from 15 August to 15 September 2010.

3. Impact of dropsondes on the analysis and forecast

Dropsondes were released within the storm and its vicinity during PREDICT. Because the dropsonde quality is considered high, it is interesting to briefly evaluate their impact on the analysis and forecast of Hurricane Karl without ARO observations first, that is, the CTRL experiment versus the G experiment.

As seen in Fig. 2a (the CTRL experiment), the impact of dropsonde as well as radiosonde soundings on total precipitable water (TPW), defined as column-integrated

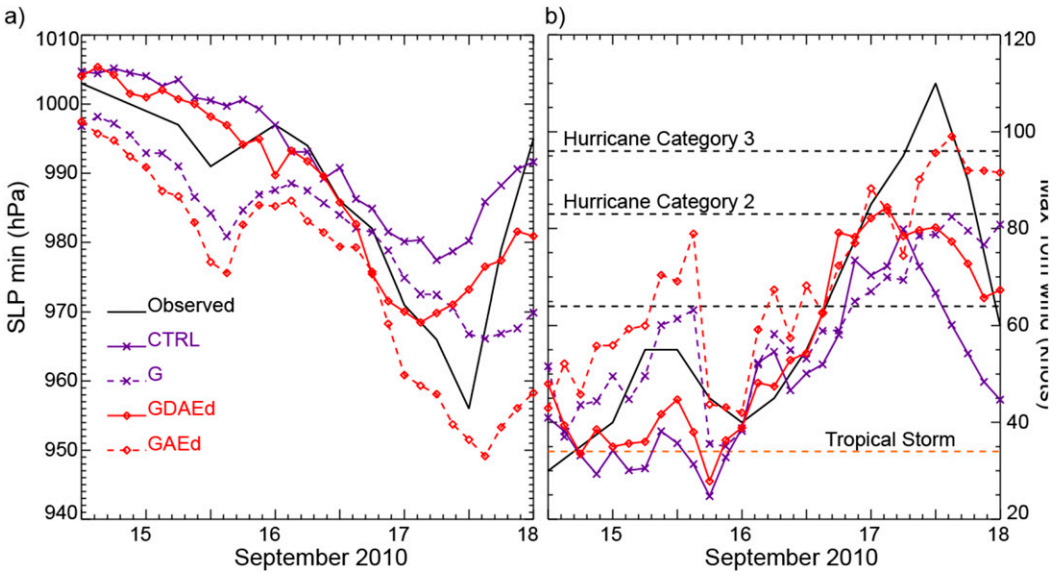

FIG. 3. Evolution of the simulated storms with (CTRL and GDAEd) and without (G and GAEd) dropsondes assimilated in domain 3 (colored lines) vs the observed (black line): (a) minimum central SLP (hPa) and (b) maximum 10-m wind speed (kt). The Saffir–Simpson tropical storm (TC) and hurricane categories (1–3) wind scales are indicated by the horizontal dashed lines.

water vapor, is dominant over that of other GTS point observations at the analysis time. There was an increase (decrease) in TPW on the north (south) side of the storm center, and it is noted that the negative increments in moisture throughout the column south of the storm are larger in magnitude. Meanwhile, a slight increase in low-to-midlevel pressure occurred south and southeast of the storm (figures not shown). As a result, the predicted storm became weaker (Fig. 3). As observed from the comparison between the CTRL and G experiments, the assimilation of dropsondes (CTRL) mainly contributed to the forecast correction of the otherwise overintensifying storm (G), especially at the early stages of storm development, even though the corrected storm is now weaker than observed.

4. Impact of the airborne radio occultations on the analysis

As seen from Eq. (1), the model variables that are directly affected by the assimilation of ARO observations are water vapor content, air temperature, and air pressure. Wind variables are indirectly affected through the multivariate background error covariance and the penalty function (i.e., the balance equation) during minimization of the cost function. Below, in addition to the general discussion of the impact of ARO observations on the analysis, our discussion focuses on two aspects: 1) the analysis differences between local refractivity experiments and nonlocal EPH experiments and 2) the influence of horizontal tangent point locations (i.e., drifting vs nondrifting) on the analysis.

a. Moisture analysis and comparison between local (N) and nonlocal (EPH) operators

Figure 2b shows the additional impact from the assimilation of nondrifting ARO local refractivity in the GDANn experiment with respect to CTRL. Nondrifting ARO refractivity further reduced TPW by up to 5 mm over western Cuba, Haiti, and the Dominican Republic while further increasing TPW (~2 mm) over Jamaica and off the coast of Colombia around 12°N, 72°W.

In comparison, the impact of ARO nondrifting excess phase (GDAEn) on TPW with respect to CTRL is shown in Fig. 2d. Two main differences are noted with respect to the impact seen in GDANn. First, the impact regions from the assimilation of ARO excess phase are elongated in the direction of the ray paths, compared to the local refractivity case. This is due to the redistribution of EPH increments along the ray paths over which refractivity was integrated. Second, the increases in moisture north and southeast of the storm, and the decreases northeast and northwest of the storm, are larger in magnitude when the nonlocal EPH operator is used. These conclusions are also applicable to the drifting experiments (i.e., GDANd in Fig. 2c vs GDAEd in Fig. 2e)

To better illustrate the difference between the two operators, Fig. 4 shows the assimilation of a single ARO profile to the northwest of the storm (PRN13 in Fig. 2d)

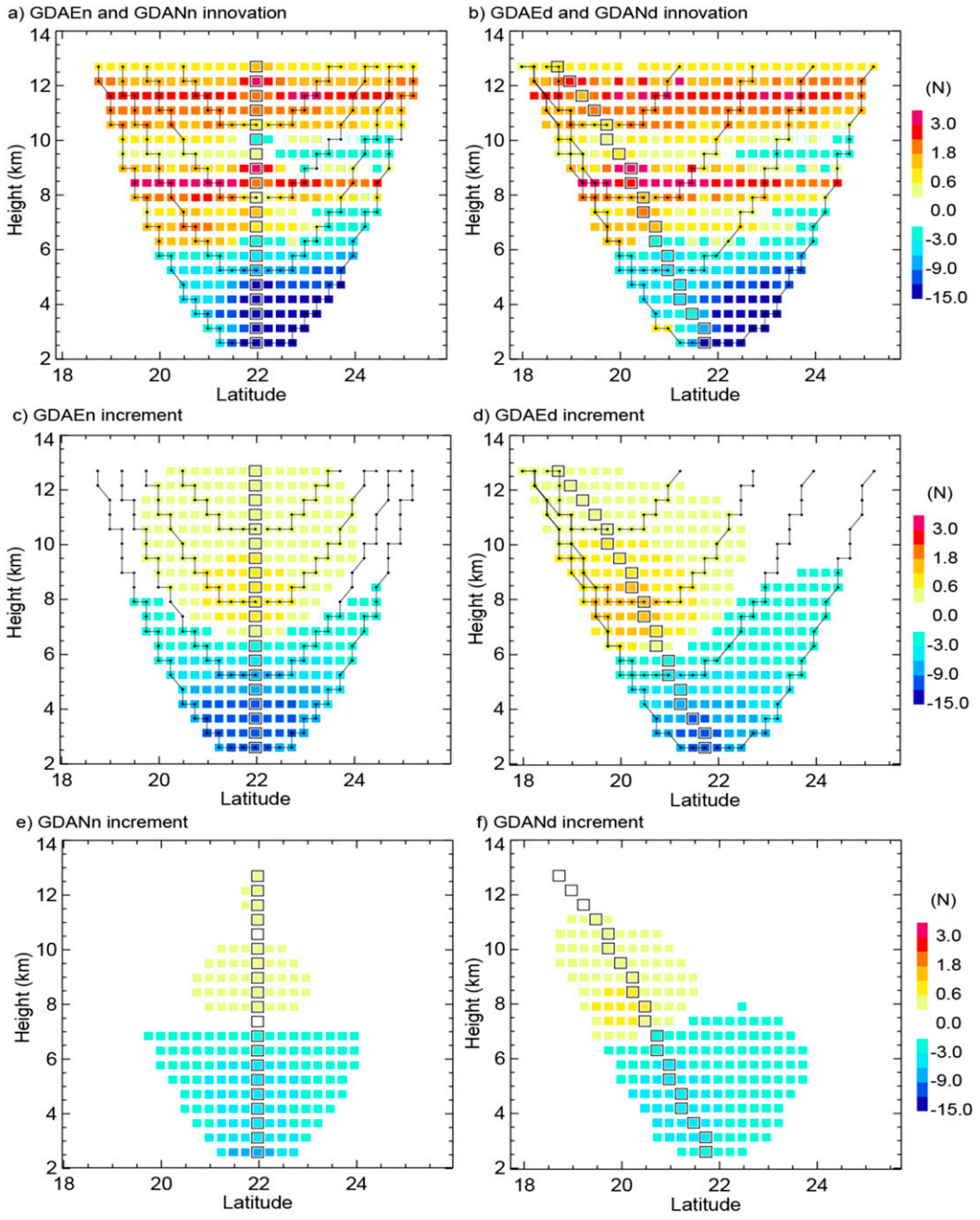

FIG. 4. (a),(b) Domain 2 innovation (observation − model background) in refractivity of PRN13 at the tangent points and along (a) nondrifting and (b) drifting ray paths. Four ray paths are shown as examples by thin squiggly black lines. These line paths bend upward when plotted relative to the earth's surface. Innovations for the GDAN local refractivity experiments occur only at the tangent points (black rectangles, □), whereas for the GDAE experiments, they occur along the entire ray path. (c)–(f) Increments (analysis − model background) after the first OL iteration of minimization along ray paths from DA of PRN13, using the (c) nondrifting and (d) drifting EPH operator vs the (e) nondrifting and (f) drifting local refractivity operator. The innovation and increment along each ray, as well as tangent points, are plotted as projected onto the two-dimensional latitude–height plane.

using the two operators. As mentioned earlier, PRN13 is shown here because it had an important impact on the forecast of Hurricane Karl's rapid intensification, which will be discussed in section 5b. Plotted in Figs. 4a and 4b are the innovation in refractivity along the ray path (black line), assuming no tangent point drift and tangent point drift, respectively. Innovation is defined as the difference between the one-dimensional observations and the three-

dimensional model background interpolated to the ray path points. Note that in this exercise of single profile assimilation, only one outer-loop iteration was performed during minimization to simplify the analysis. The asymmetry of the refractivity innovation reflects the inhomogeneity of the model refractivity along the ray paths. In the case of this profile, the model background overestimated refractivity, compared to observations below 6 km, especially on the northern portions of the rays where the model was relatively wet (not shown). The innovation of each ray at the tangent points (boxed pixels in Figs. 4a,b) is also the innovation of local refractivity, while the integration of the refractivity innovations along individual ray paths gives the innovation of EPH. The main difference noted here between local refractivity and EPH operators is because of the integration over ray paths. The total increment from the assimilation of EPH (Figs. 4c,d) is redistributed along the rays, thus giving a larger impact area than local refractivity (Figs. 4e,f) in the direction of the ray paths.

While previous studies have examined the difference between results of a local versus nonlocal radio occultation observation operator, this is the first case where the density of profiles has been sufficient that regions over which the EPH operator has been applied have overlapped. Six profiles near the storm center have overlapping lines of sight, so, for example, comparing Figs. 2d and 2e illustrates that there are significant differences in the near-storm region at relatively small spatial scale and, in particular, at a spatial scale that is less than the horizontal scale of an individual observation.

b. *Effect of the horizontal drifting of tangent points*

One distinct characteristic of ARO measurements is the large horizontal drift in the position of the tangent points within one occultation profile, 2 to 3 times that of spaceborne observations. This spreads further the 3D sampling of the volume in the near-storm region, so it is interesting to analyze the impact of the tangent point drift on Karl's analysis and forecasts. Here, only EPH experiments will be compared and discussed (i.e., GDAEn vs GDAEd).

Compared to the CTRL experiment, most of the changes in TPW tend to be slightly larger at the occultation locations when nondrifting ARO observations are assimilated, compared to drifting ARO (Fig. 2b vs Fig. 2c and Fig. 2d vs Fig. 2e). It is partly due to the vertically accumulated impact over the same vertical column in GDANn (Fig. 2b) and GDAEn (Fig. 2d), while the impact in GDANd (Fig. 2c) and GDAEd (Fig. 2e) is spread out in both the horizontal and vertical along the tangent point drift direction. Most differences seen between GDAEn and GDAEd are due to variability along the tangent point drift direction in the model background fields. For example, when examining the values of refractivity innovation along the rays and at the tangent point locations (black boxes in Figs. 4a,b) for the PRN13 profile northwest of the storm analyzed earlier, it is seen that GDAEd had smaller negative innovations than GDAEn below 6 km, as the rays from the tangent points are displaced southeastward. The model became drier in the southeast direction, toward where the tangent points were displaced (figure not shown). Therefore, even though the assimilation of drifting excess phase (Fig. 4d) still resulted in negative increments in refractivity and moisture near the surface, as in the nondrifting case (Fig. 4c), it is of smaller magnitude, and positive increments are larger in the mid-to-upper levels.

We further note from Fig. 2e that in the three profiles that gave positive increases in moisture north and southeast of the storm, the tangent points at higher levels drifted closer to the storm center. Moreover, moisture increments were, in general, the greatest between 700 and 500 hPa. Consequently, the assimilation of drifting ARO EPH observations resulted in larger increases in moisture in the vicinity of the storm at middle levels (e.g., between Jamaica and the storm center), compared to the nondrifting GDAEn experiment (Fig. 5b vs Fig. 5a), which may favor storm development.

c. *Impact on pressure and wind*

The assimilation of ARO observations changed pressure in a manner very similar to moisture, as one may expect from Eq. (1). The changes in pressure would, in turn, force an indirect change in the wind field through the correlation in the background error covariance and through the balance equation as part of the minimization process. The temperature increment at low levels was very small (figure not shown) and thus had negligible impact on the wind.

The impact of local refractivity (GDANn) was relatively small on both pressure and wind (Figs. 6a,d) and likely had a minor impact on the forecast. In the case of EPH (GDAEn and GDAEd), a small local pressure gradient was created from an increase in pressure north of Columbia and Venezuela and from decreases in pressure south of the storm center and east of the storm, near Jamaica (Figs. 6b,c). The resulting change in the wind field was a clockwise motion southeast of the storm up to 0.4 m s^{-1} at the 3-km level (Figs. 6e,f), giving a positive vorticity anomaly due to the shear effect, and thus, a positive vorticity advection immediately east-southeast of the storm (Figs. 6b,c). This may have had an impact on the forecast of Hurricane Karl's

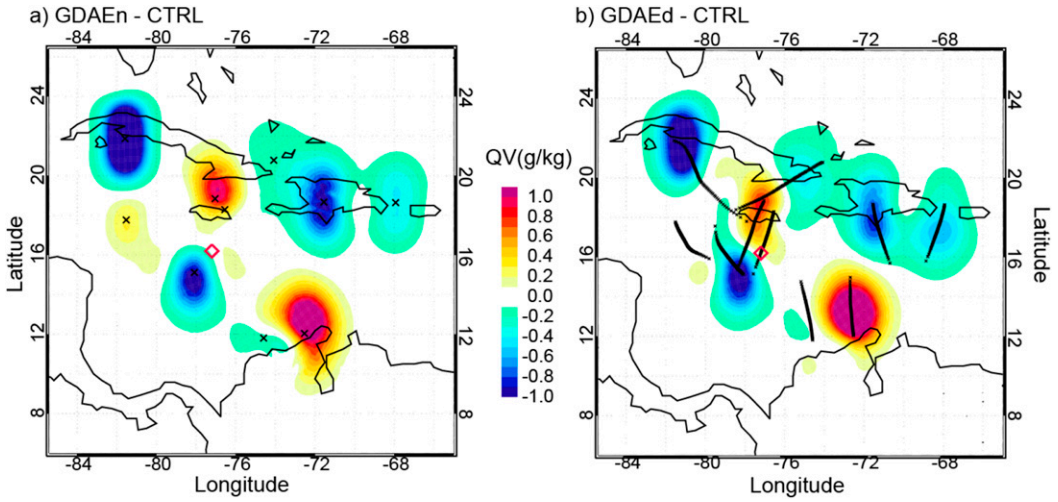

FIG. 5. The analysis differences of the 600-hPa water vapor mixing ratio (color shaded in $g\,kg^{-1}$) at 1200 UTC 13 Sep in domain 2 for (a) GDAEn − CTRL and (b) GDAEd − CTRL. The small black × symbols in (a) indicate the position of the assimilated airborne RO tangent points at ~2 km. The red diamonds indicate the estimated position of the cyclone from the NCEP Tropical Cyclone Vitals Database.

rapid intensification later. Although there was negative vorticity advection farther southeast of the storm, which could have had a negative impact on the storm development, it was also accompanied by a favorable condition of a deeper moist layer.

5. Impact of the airborne radio occultations on the forecast

The significant features of Hurricane Karl's development were successfully reproduced by the numerical forecasts in our study when GPS ARO data were assimilated properly (e.g., GDAEd). These include Hurricane Karl's rapid intensification after crossing the Yucatan Peninsula and its dominant westward trajectories (Fig. 7). The experiments where ARO observations with drifting tangent points were assimilated distinguished themselves in simulating stronger hurricanes that were closer to the observed intensities, and their tracks were farther south and closer to the observed track prior to and during the passage over the Yucatan Peninsula and in the southern Gulf of Mexico.

a. Analysis of the forecasts before rapid intensification

Genesis occurred in all experiments but was slightly weaker than observed when dropsondes were assimilated (i.e., CTRL vs G and GDAEd vs GAEd). Note that we have defined genesis to occur when the maximum 10-m wind speed within a 200-km radius of the storm center reaches the tropical storm strength, which is $17.5\,m\,s^{-1}$ or 34 kt ($1\,kt = 0.51\,m\,s^{-1}$) in the Saffir–Simpson hurricane wind scale. Prior to crossing the Yucatan Peninsula, the surface low and the midlevel vortex remained weak for the first 2 days of the forecast in all experiments that incorporated dropsondes. During that time, the forecast storm intensity was weaker than observed (Figs. 7a,b). The only exceptions were experiments that did not assimilate dropsondes, in which case genesis was too early, and the intensity was greatly overpredicted (i.e., G and GAEd in Fig. 3).

In the case of the GDAEn and GDAEd simulations where ARO EPH observations were assimilated, even though the intensity of the storm remained similar to the other experiments, the vortex was noted to be more compact during the early development. This is likely due to the increase in midlevel moisture in the vicinity of the storm (Fig. 5) and positive vorticity advection (Figs. 6b,c), which favored storm development. A comparison between model and satellite TPW observations at later times indicates that the model background indeed underestimated the column moisture (e.g., off the north coast of Colombia) (Fig. 8), supporting the idea that the initial moisture field in that region was improved after the assimilation of ARO EPH observations. The satellite composite shows significantly more moisture between the storm center and Panama than the simulations because neither the GTS observational dataset nor the ARO observations sampled this region.

A sensitivity test (figures not shown) was further conducted to investigate the importance of the changes in the initial moisture field from the assimilation of ARO EPH on the forecast. For this test, the water vapor mixing ratio field at the analysis time of the GDAEd

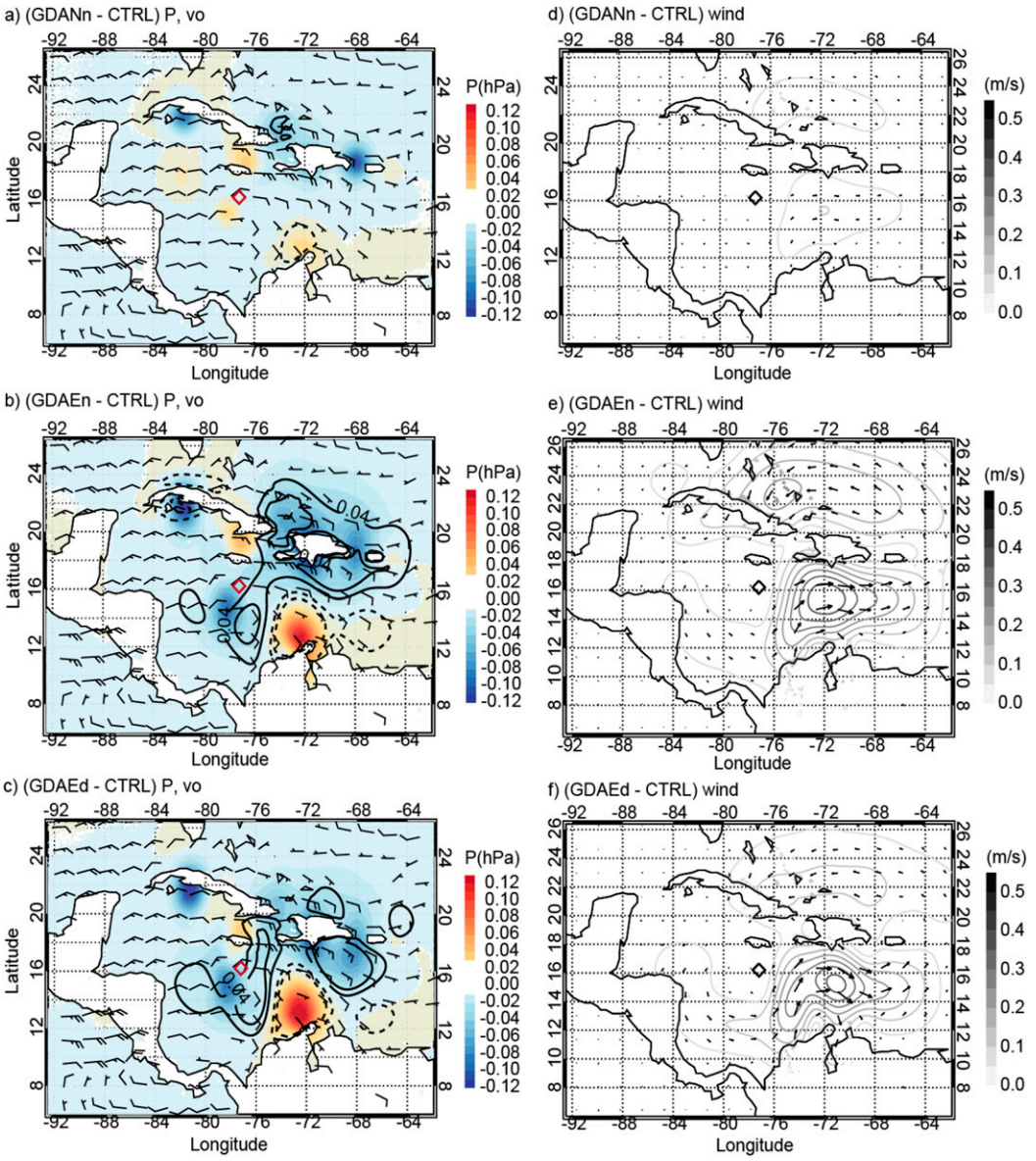

FIG. 6. The analysis differences of 3-km pressure (color shaded in hPa) and relative vorticity (positive in solid contours, negative in dashed at 0.04×10^{-5} s^{-1} intervals) at 1200 UTC 13 Sep in domain 2 of (a) GDANn − CTRL, (b) GDAEn − CTRL, and (c) GDAEd − CTRL. The 3-km wind field of the simulations with ARO assimilated are plotted as wind barbs. (d)–(f) Wind speed (contours) and vector differences at the 3-km height between the same experiments as in (a)–(c), respectively. Arrows indicate the directional difference, and 0.05 m s^{-1} interval contours are the magnitude of the difference. The diamonds indicate the estimated position of the cyclone from the NCEP Tropical Cyclone Vitals Database.

experiment was replaced by that of the CTRL experiment. The resulting cyclone was similar to CTRL in intensity while much weaker than the original GDAEd experiment and the real cyclone, further supporting the hypothesis that the increments of midlevel moisture were important. This finding agrees with an earlier study by Torn and Cook (2013), where the authors also found that the 48-h forecasts of Hurricane Karl were particularly sensitive to initial midlevel moisture perturbations southeast of the storm, north of Colombia and Venezuela. Davis and Ahijevych (2013) reached similar conclusions about the importance of midlevel moisture in developing storms sampled during PREDICT from dropsonde observations.

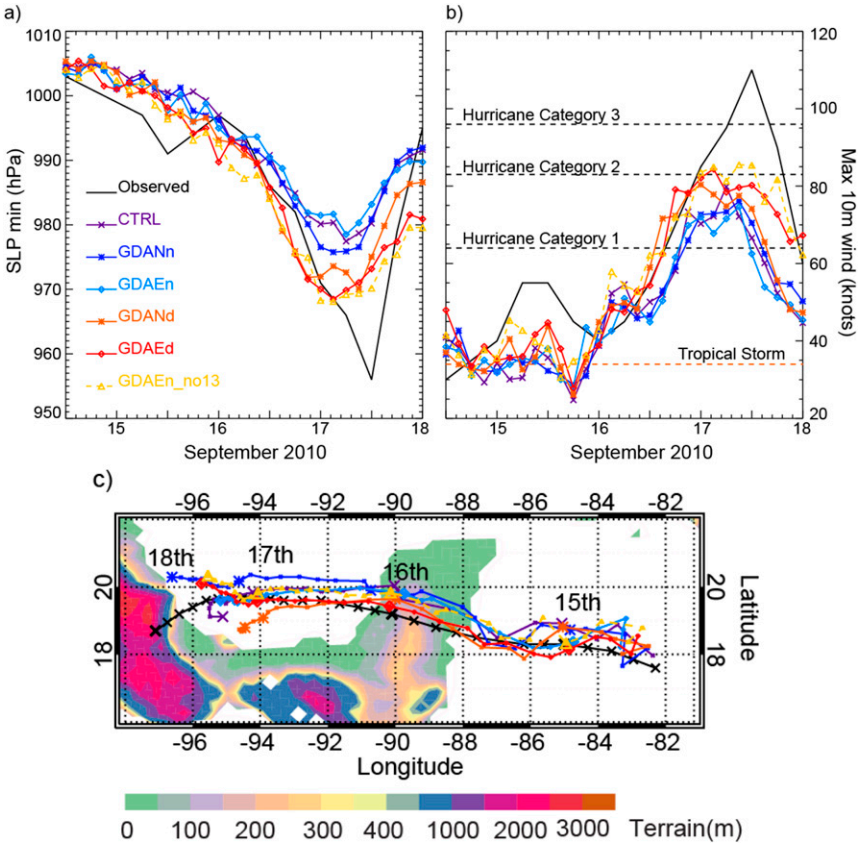

FIG. 7. Evolution of the simulated storms in domain 3 (colored lines) vs the observed (black line): (a) minimum central SLP (hPa) and (b) maximum 10-m wind speed (kt). The Saffir–Simpson tropical storm (TC) and hurricane categories (1–3) wind scales are indicated as horizontal dashed lines. (c) Track of the surface minimum SLP center from 1200 UTC 14 Sep to 0000 UTC 18 Sep 2010 (time of observed landfall). Track positions at 0000 UTC are indicated by the large symbols. Note that results from CTRL and GDAEd, which were plotted in Fig. 3, are replotted again here for reference.

Landfall over the Yucatan Peninsula did not show as much impact in the simulated storms as it did in the observed intensity of Hurricane Karl. Even though the terrain of the peninsula is lower than 400 m, the observed surface low weakened by around 5 hPa during the passage over the land between 1200 UTC 15 September and 0300 UTC 16 September. However, in all forecasts, both the surface low and the midlevel vortex continued to strengthen over land after a brief halt and a short decrease in surface wind speed due to the surface friction.

During the passage over the peninsula, the storms in all experiments moved along west-northwestward trajectories, similar to the observed track (Fig. 7c). Previous studies (e.g., Adem 1956; Elsberry 1995) have shown that cyclone propagation is primarily determined by the environmental flow and can be further influenced by other external and internal forcings. The environmental flow in this case was the anticyclonic circulation of the subtropical ridge north of the developing cyclone, which was noticed to be weaker in all the forecasts compared to the ERA-Interim.

b. *Analysis of the forecasts during and after rapid intensification*

Similar to the observed cyclone, but 3 h earlier, the simulated storms started intensifying at around 1800 UTC 15 September as they moved over the warmer sea surface temperature and humid environment of the Gulf of Mexico. The storms in the CTRL, GDANn, and GDAEn experiments reached category 1 hurricane intensity at about 1800 UTC 16 September, then weakened as they approached the coast of Mexico. The storm in GDANd almost reached category 2 intensity at 0000 UTC 17 September, whereas GDAEd reached category 2 intensity at 0300 UTC 17 September, being the closest one to the actual category 3 Hurricane Karl (Fig. 7b).

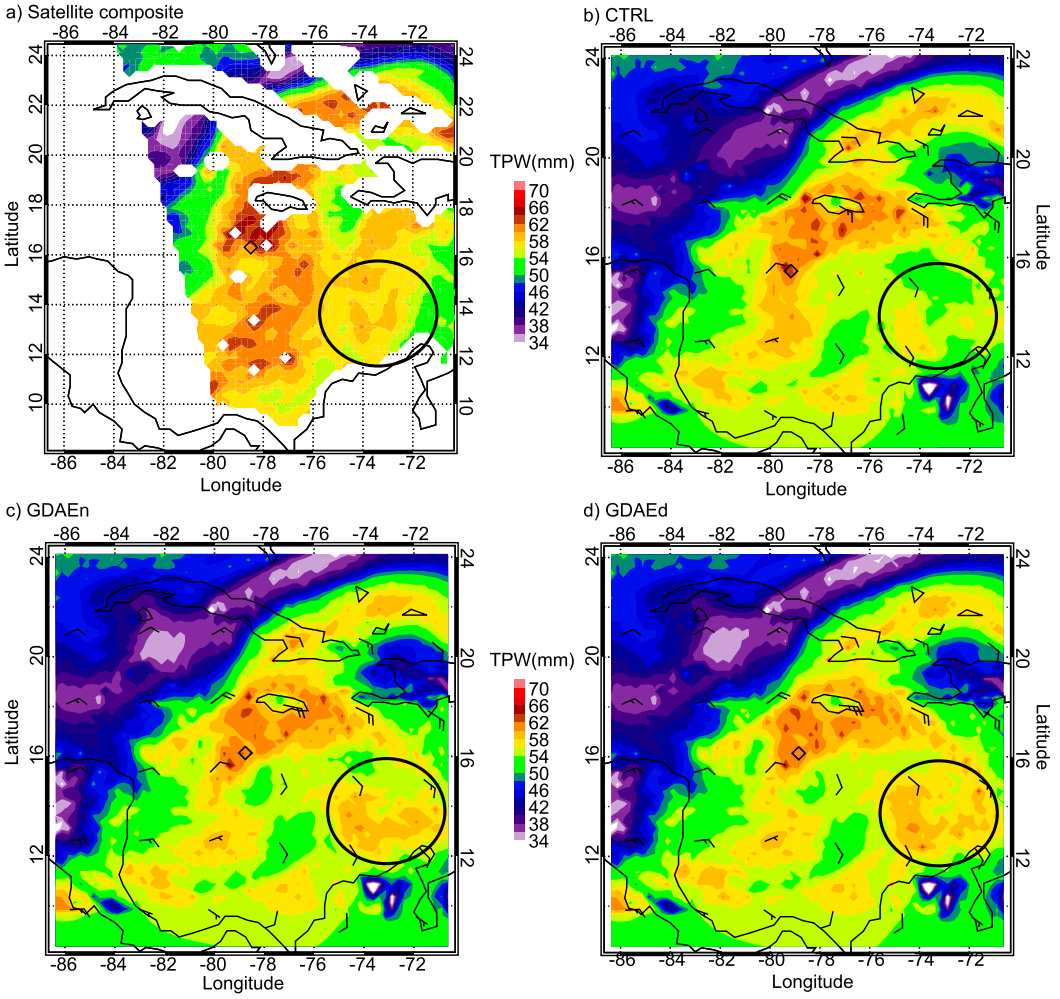

FIG. 8. (a) Composite of satellite microwave observations of TPW at 1800 UTC 13 Sep. (b)–(d) Simulated TPW fields from domain 3, regridded to the same spacing as satellite observations (0.25°) using inverse distance-weighted averaging for the CTRL, GDAEn, and GDAEd experiments, respectively, at 1800 UTC 13 Sep. The 900–400-hPa mass-weighted average mean flow is plotted in wind barbs. Black diamonds indicate the (a) observed and (b)–(d) simulated positions of the cyclone at the plotted time. The satellite data in (a) include those from the Special Sensor Microwave Imager (SSM/I *F*15–17) on board the Defense Meteorological Satellite Program (DMSP) satellites, the Advanced Microwave Scanning Radiometer (AMSR-E) on *Aqua*, the Tropical Rainfall Measuring Mission's (TRMM) Microwave Imager (TMI), and the WindSat Polarimetric Radiometer on the Coriolis satellite. Black ellipses indicate the moist area better captured after assimilation of ARO EPH observations, and the white areas in (a) are missing data.

The experiments where drifting tangent points were assimilated captured the RI better than the other simulations yet did not reach category 3. Recall that dropsondes helped correct the over-intensification of the storm during the first 2 days, even though it resulted in a weaker storm than observed (i.e., G vs CTRL). The drifting ARO EPH observations in GAEd improved the intensification rate during the later RI period, but the storm overintensified without the dropsondes (i.e., G vs GAEd). It is the combination of both datasets (i.e., in GDAEd) that helped correct the prediction of storm intensity and improved the RI rate.

Close to the final landfall, a southward turn was observed in Karl's propagation on early 17 September. From observations, it was hypothesized that the turning was due to a strengthening of the subtropical ridge that extended to the south (Stewart 2011). The feature was not captured in the forecasts, where the ridge instead weakened on late 16 September (figures not shown). This is likely due to the effect of higher vertical shear and entrainment of dry air from the approaching continental air into the storm environment. All the forecasts of Hurricane Karl started to weaken in intensity early on 17 September while the storm slowed.

c. Analysis of dry air intrusion to rapid intensification

In both experiments where ARO EPH observations were assimilated (i.e., GDAEn and GDAEd), bands of dry air at middle levels were wrapped around the storm by its own cyclonic circulation, shown by blue shading of low water vapor content in Fig. 9. The dry area is closer to the storm vicinity in the GDAEn experiment (Figs. 9a,b) than in GDAEd (Figs. 9c,d), and the storm in GDAEd is slightly better organized at 0000 UTC 16 September (Fig. 9d). Studies have shown that midlevel dry air intrusion enhances evaporative cooling from hydrometeors and suppresses convection (e.g., Fritz and Wang 2013; Braun et al. 2012), suggesting that we should expect less convection in GDAEn. Areas of diabatic cooling at the middle levels are indeed seen in the GDAEn experiment at 0000 UTC 16 September, near the convective clouds at the downshear side ahead of the storm within the radius of maximum 10-m wind (RMW) (Fig. 9b; black ellipse), further indicating the presence of dry air intrusion. Using 14 cases of intensifying and steady-state tropical cyclones, Rogers et al. (2013) have shown that the presence of more convective bursts on the downshear side of the storms within RMW is one of the distinct indicators of an intensifying cyclone. Guimond et al. (2016) analyzed in detail the convective bursts associated with the rapid intensification of Karl from satellite infrared images, 1-km retrievals of airborne Doppler radar wind measurements, and coincident upwelling radiation measurements from an airborne sounding radiometer during the Genesis and Rapid Intensification Processes (GRIP) field campaign. Their findings agreed with Rogers et al. (2013), where deep convection was present mostly downshear of Hurricane Karl. It is thus suggested that convective activity was suppressed ahead of the GDAEn storm due to the presence of dry air at the midlevels, affecting the storm's rapid intensification.

Following up on the dry air intrusion, two questions arise: Where did the dry air come from, and why did the assimilation using nondrifting tangent points weaken Karl's RI rate, compared to the case with drifting tangent points? To identify the origin of the drier air mass in GDAEn where strong diabatic cooling occurred (see black ellipse in Fig. 9b), backward trajectories were performed from 0000 UTC 16 September back to the analysis time at 1200 UTC 13 September (Fig. 10). Six air parcels were placed in that diabatic cooling region at different pressure levels between 550 and 700 hPa. The results in Fig. 10 show that many of these dry air parcels came from western Cuba at the analysis time, which coincide with the increased negative moisture anomaly area from the assimilation of the ARO occultation PRN13 in GDAEn (Fig. 2d) relative to GDAEd (Fig. 2e).

d. Sensitivity test of the PRN13 profile

The PRN13 profile had a significantly longer tangent point drift distance than did the other observations, as mentioned earlier. This had a significant effect on the GDAEn result, which did not take into account this drift, and resulted in a larger, incorrect reduction of total column moisture, compared to the GDAEd experiment (Fig. 2d vs Fig 2e). It is thus suggested that the drier air mass affecting the storm in GDAEn is a result of the larger decrease in moisture in the assimilation of nondrifting EPH of the PRN13 profile. To test this hypothesis, a sensitivity test (GDAEn_no13) was conducted where the particular profile (PRN13) was removed during DA. Indeed, the areas of diabatic cooling, indicative of dry air intrusion and thus, evaporation, immediately west of the storm center (black ellipses in Figs. 9a,b) are absent in the GDAEn_no13 experiment (Figs. 9e,f; Fig. 11c). Even though areas of diabatic cooling are seen around the storm in GDAEd and GDAEn_no13 (Figs. 9c–f), which is to be expected, considering the bands of dry air wrapping around the storm, they are of smaller extent and are farther away from the storm.

Concurrently, the vortices at 850 and 500 hPa in GDAEd and GDAEn_no13 were vertically aligned, as well as aligned with the center of minimum sea level pressure (SLP) (Figs. 11b,c) at 0000 UTC 16 September after the storm crossed the Yucatan Peninsula, while those in GDAEn were misaligned (Fig. 11a). Thus, the midlevel dry air intrusion seen in GDAEn, combined with a vertical misalignment of the storm structure, likely explains why a weaker intensification rate was obtained after 0000 UTC 16 September for GDAEn, compared to GDAEd and GDAEn_no13 (Fig. 7a). The latter experiments (i.e., GDAEd and GDAEn_no13) intensified at a rate more comparable to observations, though the RI did not last long enough to capture Hurricane Karl's minimum sea level pressure. The GDAEn_no13 experiment highlights the importance of the midlevel moistening near the storm, as exhibited by GDAEd. This implies that even if the excess phase is a better observation operator, assimilation of such data with incorrect tangent point locations might introduce significant errors in the analysis, which then degrade the forecast.

6. Summary and discussion

In this case study of Hurricane Karl in 2010, three aspects of the assimilation of ARO observations were investigated: 1) the impact of the observations on the initial conditions and forecasts in comparison to dropsondes under the absence of satellite observations, 2) the impact of using the nonlocal EPH operator as compared to local

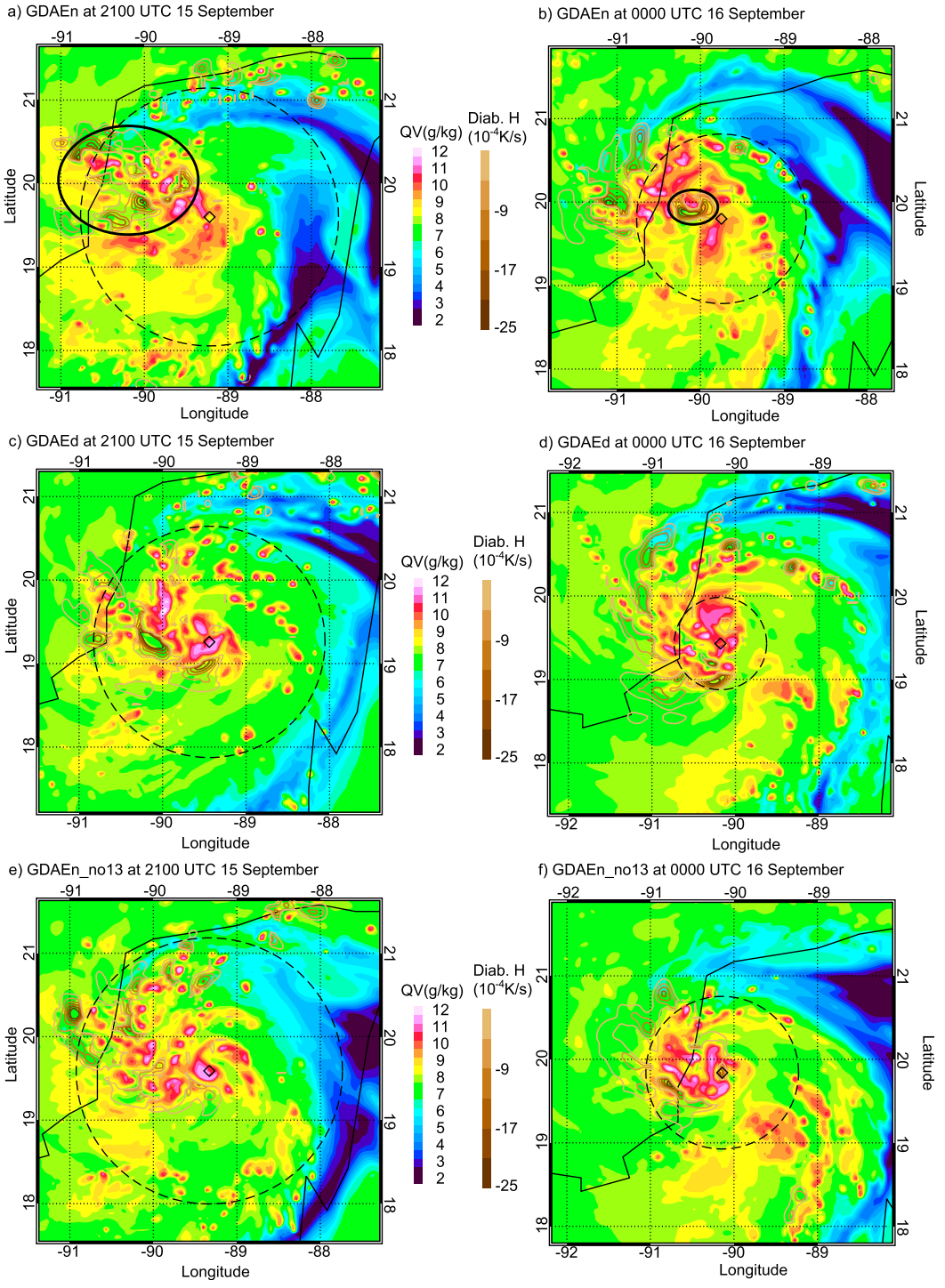

FIG. 9. (a),(b) Water vapor mixing ratio (color shading) and diabatic heating (brown contours) at 650 hPa of GDAEn at 2100 UTC 15 Sep and 0000 UTC 16 Sep, respectively. (c),(d) Same for GDAEd and (e),(f) same for GDAEn_no13. Black diamonds indicate the position of the model minimum SLP. Dashed circles are the radii of maximum 10-m winds. The black ellipses in (a),(b) indicate the areas of diabatic cooling ahead of the storm that likely impeded the storm's development.

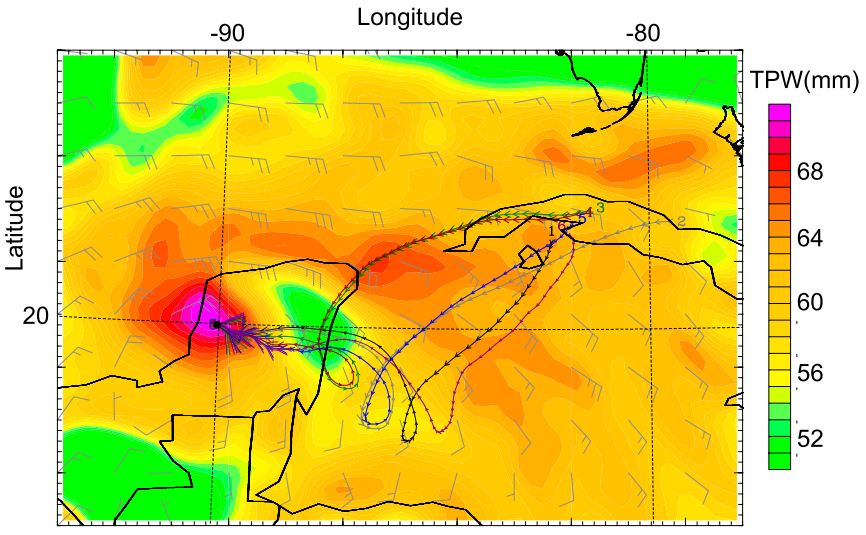

FIG. 10. Backward trajectories in the nonmoving parent domain (27-km grid spacing) of six air parcels in the GDAEn experiment from 0000 UTC 16 Sep to 1200 UTC 13 Sep (analysis time). At 0000 UTC 16 Sep, the parcels were sampled within the same column (black dot) at different levels between 550 and 700 hPa with an interval of 50 hPa near the storm center, where strong adiabatic cooling occurred (see the ellipse in Fig. 9b). TPW (mm) at 0000 UTC 16 Sep is plotted in color contours.

refractivity, and 3) the sensitivity of the simulations to the drifting of the tangent points within the ARO profiles. Depending on the operator used to assimilate the ARO observations (i.e., refractivity vs EPH), their impact on Hurricane Karl's forecast ranged from neutral to positive. Overall, the forecasts were mostly sensitive to the positioning (drifting vs nondrifting) of the ARO tangent points during DA, whereas the analyses were mostly impacted by the type of operator used (local vs nonlocal).

The assimilation of dropsondes corrected Hurricane Karl's over-intensification during the first 48-h forecast. In comparison, ARO observations mainly impacted the rapid intensification period (72–96-h forecast). This is likely because dropsonde soundings improved analysis within and near the storm, while ARO observations, due to their side view from the aircraft, also improved the broader storm environment, which in turn influenced the storm's development at a later time.

The assimilation of local refractivity, drifting or not, brought very little impact on the initial conditions, in addition to the conventional and dropsonde observations. Geometrically, the impact of considering drift in GDANd had a tendency to spread out the impact in both the horizontal and vertical along the tangent point drift direction, relative to the nondrifting GDANn simulation, giving a smaller impact on TPW, pressure, and winds. Compared to local refractivity, the assimilation of ARO EPH produced similar patterns, but with larger increments that extended farther along the ray paths.

In the experiments that assimilated ARO EPH, improvements in the forecast can be explained by increments seen at the analysis time. Increases in moisture in the inflow region, especially at midlevels, and an increase of cyclonic vorticity at analysis time acted together to help the cyclone keep a stronger upper-level circulation as the storm crossed the Yucatan Peninsula. The smaller decrease in moisture over western Cuba from analysis time in the drifting tangent point case, GDAEd, compared to GDAEn, helped reduce dry air intrusion into the storm at the beginning of its rapid intensification phase. Furthermore, the dry air intrusion in GDAEn caused evaporative cooling, which suppressed convection ahead (downshear) of the storm. This in part explains why the rapid intensification was weaker in GDAEn than in GDAEd. In addition, a better vertical alignment of the vortex right before rapid intensification was seen in GDAEd. Of the simulations that included both dropsondes and ARO profiles, GDAEd allowed the storm to develop into the strongest simulated hurricane and the one closest to the observations.

The impact of tangent point drift seen in the experiments suggested that the correct positioning of the ARO observations is important. In particular, the impact from the PRN13 profile in the outer circulation of the storm was large. Similar situations were found in spaceborne RO studies (e.g., Chen et al. 2009; H. Liu et al. 2012), where a small subset of profiles was critical to the impact on the storm forecasts. Because ARO observations can

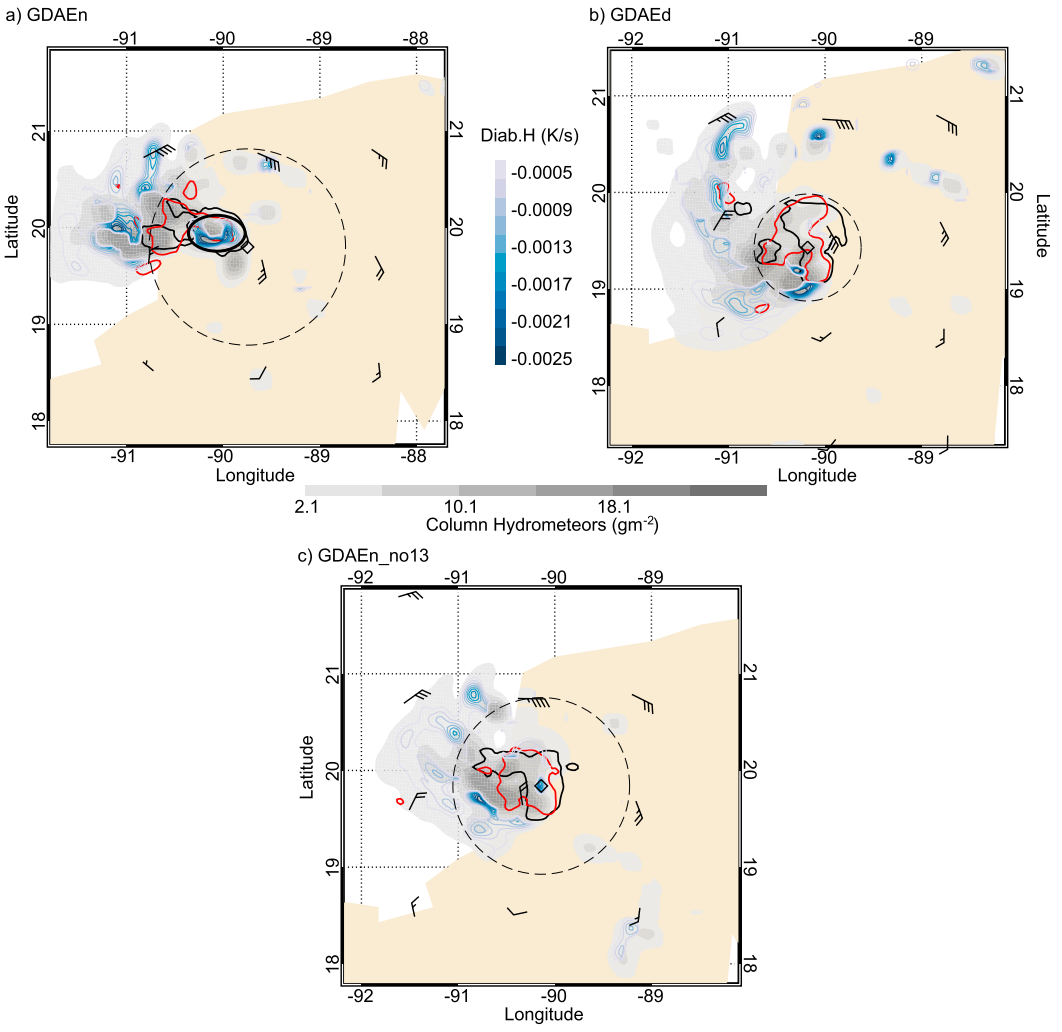

FIG. 11. Gray shading contours of column-integrated mixing ratio of hydrometeors (cloud, rain, snow, ice, and graupel) in g m^{-2} in domain 3 for (a) the GDAEn experiment, (b) the GDAEd experiment, and (c) the GDAEn_no13 experiment at 0000 UTC 16 Sep 2010, with diabatic heating at 650 hPa (blue contours), relative vorticity at 500 (red) and 850 hPa (black), and the 900–400-hPa mass-weighted average mean flow in wind barbs. Black diamonds indicate the NHC estimate of the cyclone surface center. Dashed circles indicate the radius of maximum 10-m wind speed. The black ellipse in (a) indicates the same area of diabatic cooling as in Fig. 9b.

be denser than spaceborne RO observations over a targeted region, they have a higher chance of capturing a sensitive area of the storm environment. This also makes the use of the proper assimilation method for ARO observations even more important.

Even though there were no ARO observations assimilated below 2 km due to low signal-to-noise ratio and therefore, low data quality, the impact of the observations above 2 km extended down to the surface. This is due to the vertical covariance of the background error, which was calculated using the method of empirical orthogonal functions (Barker et al. 2004). This introduces a potential representativeness error in the results of assimilation because moisture can be highly variable at low levels. A desirable future improvement is to improve the antenna gain to increase the signal-to-noise ratio of ARO measurements near the surface, which would allow deeper retrievals down to the surface and potentially have a larger impact on improving numerical forecasts of hurricanes.

The conclusions reached in this study are based solely on one case study. To draw more general conclusions, more case studies are required as more ARO observations become available. However, one case study is very useful for indicating the regions of the storm that are most sensitive to this type of geometry (midlevels) and the spatial extent that is affected, in order to plan further assimilation experiments. We further note that excluding satellite radiance observations in the data assimilation

may have caused an overestimation of the observational impact for both dropsondes and ARO data. In addition, observation representativeness errors specific to the model resolution were not assessed in this case study and should be further investigated in future studies if the ARO observations are to be used in an operational setting and as more cases with ARO data become available. With the launch of additional constellations of navigation satellites, including Galileo and Beidou, denser spaceborne GPSRO datasets can also be expected. Finally, it would also be interesting in the future to evaluate the impact of ARO observations using a hybrid or an ensemble DA method with a flow-dependent background error covariance.

Acknowledgments. This study was primarily supported by the National Science Foundation (NSF) Grant 1015910 and partly supported by NSF Grants 1301835 and 1137306 and NASA Grants NNX12AK30G and NNX12AQ86G. Partial support for B. Murphy was provided by the Ross Fellowship. L. Adhikari and F. Xie were supported by NSF Grant AGS-1262041. We would like to acknowledge high-performance computing support from Yellowstone (ark:/85065/d7wd3xhc) provided by NCAR's Computational and Information Systems Laboratory, sponsored by the National Science Foundation (university allocations 36131033 and UCDV0003). We would like to acknowledge P. Muradyan and A. Johnson, who assisted with the airborne GNSS Instrument System for Multistatic and Occultation Sensing (GISMOS) data collection and preliminary analysis used in this study. We thank J. Jensen, J. Meitin, A. Cooper, A. Schanot, R. Sherman, and the NCAR–EOL and NCAR–RAF staff for their logistical support during the PREDICT campaign; and M. Bell, D. Raymond, and C. Lopez, who assisted with GISMOS operation. We also acknowledge M. Montgomery and C. Davis for providing the opportunity to participate in the PREDICT field campaign. The GTS conventional observations were provided by the Data Support Section of the Computational and Information Systems Laboratory at NCAR. The satellite data used for verification were provided by Remote Sensing Systems and sponsored by the NASA Earth Science MEaSUREs Program (available at www.remss.com). ERA-Interim data were provided courtesy of ECMWF.

REFERENCES

Aberson, S. D., A. Aksoy, K. J. Sellwood, T. Vukicevic, and X. Zhang, 2015: Assimilation of high-resolution tropical cyclone observations with an ensemble Kalman filter using HEDAS: Evaluation of 2008–11 HWRF forecasts. *Mon. Wea. Rev.*, **143**, 511–523, https://doi.org/10.1175/MWR-D-14-00138.1.

Adem, J., 1956: A series solution for the barotropic vorticity equation and its application in the study of atmospheric vortices. *Tellus*, **8**, 364–372, https://doi.org/10.3402/tellusa.v8i3.9010.

Adhikari, L., F. Xie, and J. S. Haase, 2016: Application of the full spectrum inversion algorithm to simulated airborne GPS radio occultation signals. *Atmos. Meas. Tech.*, **9**, 5077–5087, https://doi.org/10.5194/amt-9-5077-2016.

Aksoy, A., S. Lorsolo, T. Vukicevic, K. J. Sellwood, S. D. Aberson, and F. Zhang, 2012: The HWRF Hurricane Ensemble Data Assimilation System (HEDAS) for high-resolution data: The impact of airborne Doppler radar observations in an OSSE. *Mon. Wea. Rev.*, **140**, 1843–1862, https://doi.org/10.1175/MWR-D-11-00212.1.

Anlauf, H., 2016: Experiences from implementing GPS radio occultations in data assimilation for ICON. *OPAC-6/IROWG-5 Workshop*, Seggau Castle, Austria, Deutscher Wetterdienst, 1–17, http://wegcwww.uni-graz.at/opacirowg2016/data/public/files/opacirowg2016_Harald_Anlauf_presentation_138.pdf.pdf.

——, D. Pingel, and A. Rhodin, 2011: Assimilation of GPS radio occultation data at DWD. *Atmos. Meas. Tech.*, **4**, 1105–1113, https://doi.org/10.5194/amt-4-1105-2011.

Aparicio, J. M., and S. Laroche, 2011: An evaluation of the expression of the atmospheric refractivity for GPS signals. *J. Geophys. Res.*, **116**, D11104, https://doi.org/10.1029/2010JD015214.

Barker, D. M., W. Huang, Y.-R. Guo, A. J. Bourgeois, and Q. N. Xiao, 2004: A three-dimensional variational data assimilation system for MM5: Implementation and initial results. *Mon. Wea. Rev.*, **132**, 897–914, https://doi.org/10.1175/1520-0493(2004)132%3C0897:ATVDAS%3E2.0.CO;2.

——, and Coauthors, 2012: The Weather Research and Forecasting Model's Community Variational/Ensemble Data Assimilation System: WRFDA. *Bull. Amer. Meteor. Soc.*, **93**, 831–843, https://doi.org/10.1175/BAMS-D-11-00167.1.

Bauer, P., G. Radnóti, S. Healy, and C. Cardinali, 2014: GNSS radio occultation constellation observing system experiments. *Mon. Wea. Rev.*, **142**, 555–572, https://doi.org/10.1175/MWR-D-13-00130.1.

Braun, S. A., J. A. Sippel, and D. S. Nolan, 2012: The impact of dry midlevel air on hurricane intensity in idealized simulations with no mean flow. *J. Atmos. Sci.*, **69**, 236–257, https://doi.org/10.1175/JAS-D-10-05007.1.

Bruyère, C. L., G. J. Holland, and E. Towler, 2012: Investigating the use of a genesis potential index for tropical cyclones in the North Atlantic basin. *J. Climate*, **25**, 8611–8626, https://doi.org/10.1175/JCLI-D-11-00619.1.

Buontempo, C., A. Jupp, and M. Rennie, 2008: Operational NWP assimilation of GPS radio occultation data. *Atmos. Sci. Lett.*, **9**, 129–133, https://doi.org/10.1002/asl.173.

Burrows, C., 2015: Progress in assimilating radio occultation data at the Met Office. *IROWG-4*, Melbourne, Victoria, Australia, International Radio Occultation Working Group, 1–62, http://irowg.org/wpcms/wp-content/uploads/2014/05/Burrows-IROWG-4.pdf.

Camargo, S. J., A. H. Sobel, A. G. Barnston, and K. A. Emanuel, 2007: Tropical cyclone genesis potential index in climate models. *Tellus*, **59A**, 428–443, https://doi.org/10.1111/j.1600-0870.2007.00238.x.

Cardinali, C., and S. Healy, 2014: Impact of GPS radio occultation measurements in the ECMWF system using adjoint-based diagnostics. *Quart. J. Roy. Meteor. Soc.*, **140**, 2315–2320, https://doi.org/10.1002/qj.2300.

Chen, S.-H., Z. Zhao, J. S. Haase, A. Chen, and F. Vandenberghe, 2008: A study of the characteristics and assimilation of retrieved MODIS total precipitable water data in severe weather simulations. *Mon. Wea. Rev.*, **136**, 3608–3628, https://doi.org/10.1175/2008MWR2384.1.

Chen, S.-Y., C.-Y. Huang, Y.-H. Kuo, Y.-R. Guo, and S. Sokolovskiy, 2009: Assimilation of GPS refractivity from FORMOSAT-3/COSMIC using a nonlocal operator with WRF 3DVAR and its impact on the prediction of a typhoon event. *Terr. Atmos. Oceanic Sci.*, **20**, 133–154, https://doi.org/10.3319/TAO.2007.11.29.01(F3C).

——, ——, ——, and S. Sokolovskiy, 2011: Observational error estimation of FORMOSAT-3/COSMIC GPS radio occultation data. *Mon. Wea. Rev.*, **139**, 853–865, https://doi.org/10.1175/2010MWR3260.1.

Chen, Y.-C., M.-E. Hsieh, L.-F. Hsiao, Y.-H. Kuo, M.-J. Yang, C.- Y. Huang, and C.-S. Lee, 2015: Systematic evaluation of the impacts of GPSRO data on the prediction of typhoons over the northwestern Pacific in 2008–2010. *Atmos. Meas. Tech.*, **8**, 2531–2542, https://doi.org/10.5194/amt-8-2531-2015.

Choi, Y., D.-H. Cha, M.-I. Lee, J. Kim, C.-S. Jin, S.-H. Park, and M.-S. Joh, 2017: Satellite radiance data assimilation for binary tropical cyclone cases over the western North Pacific. *J. Adv. Model. Earth Syst.*, **9**, 832–853, https://doi.org/10.1002/2016MS000826.

Chou, M.-D., and M. J. Suarez, 1994: An efficient thermal infrared radiation parameterization for use in general circulation models. NASA Tech. Memo. 104606, Vol. 3, 85 pp., https://ntrs.nasa.gov/archive/nasa/casi.ntrs.nasa.gov/19950009331.pdf.

Cucurull, L., 2010: Improvement in the use of an operational constellation of GPS radio occultation receivers in weather forecasting. *Wea. Forecasting*, **25**, 749–767, https://doi.org/10.1175/2009WAF2222302.1.

——, 2012: Sensitivity of NWP model skill to the obliquity of the GPS radio occultation soundings. *Atmos. Sci. Lett.*, **13**, 55–60, https://doi.org/10.1002/asl.363.

——, and J. C. Derber, 2008: Operational implementation of COSMIC observations into the NCEP's Global Data Assimilation System. *Wea. Forecasting*, **23**, 702–711, https://doi.org/10.1175/2008WAF2007070.1.

——, ——, R. Treadon, and R. J. Purser, 2007: Assimilation of global positioning system radio occultation observations into NCEP's Global Data Assimilation System. *Mon. Wea. Rev.*, **135**, 3174–3193, https://doi.org/10.1175/MWR3461.1.

Davis, C. A., and D. A. Ahijevych, 2012: Mesoscale structural evolution of three tropical weather systems observed during PREDICT. *J. Atmos. Sci.*, **69**, 1284–1305, https://doi.org/10.1175/JAS-D-11-0225.1.

——, and ——, 2013: Thermodynamic environments of deep convection in Atlantic tropical disturbances. *J. Atmos. Sci.*, **70**, 1912–1928, https://doi.org/10.1175/JAS-D-12-0278.1.

Dee, D. P., and Coauthors, 2011: The ERA-Interim reanalysis: Configuration and performance of the data assimilation system. *Quart. J. Roy. Meteor. Soc.*, **137**, 553–597, https://doi.org/10.1002/qj.828.

DeMaria, M., J. A. Knaff, and B. H. Connell, 2001: A tropical cyclone genesis parameter for the tropical Atlantic. *Wea. Forecasting*, **16**, 219–233, https://doi.org/10.1175/1520-0434(2001)016%3C0219:ATCGPF%3E2.0.CO;2.

Elsberry, R. L., 1995: Tropical cyclone motion. *Global Perspectives on Tropical Cyclones*, World Meteorological Organization, 106–197, http://derecho.math.uwm.edu/classes/TropMet/GPTC/tcmotion.pdf.

Emanuel, K., and D. S. Nolan, 2004: Tropical cyclone activity and the global climate system. *26th Conf. on Hurricanes and Tropical Meteorology*, Miami, FL, Amer. Meteor. Soc., 10A.2, https://ams.confex.com/ams/26HURR/techprogram/paper_75463.htm.

Evans, C., and Coauthors, 2012: The PRE-Depression Investigation of Cloud-Systems in the Tropics (PREDICT) field campaign: Perspectives of early career scientists. *Bull. Amer. Meteor. Soc.*, **93**, 173–187, https://doi.org/10.1175/BAMS-D-11-00024.1.

Fritz, C., and Z. Wang, 2013: A numerical study of the impacts of dry air on tropical cyclone formation: A development case and a nondevelopment case. *J. Atmos. Sci.*, **70**, 91–111, https://doi.org/10.1175/JAS-D-12-018.1.

Gray, W. M., 1968: Global view of the origin of tropical disturbances and storms. *Mon. Wea. Rev.*, **96**, 669–700, https://doi.org/10.1175/1520-0493(1968)096%3C0669:GVOTOO%3E2.0.CO;2.

——, 1979: Hurricanes: Their formation, structure and likely role in the tropical circulation. *Meteorology over the Tropical Oceans*, D. B. Shaw, Ed., Royal Meteorological Society, 155–218.

——, 1998: The formation of tropical cyclones. *Meteor. Atmos. Phys.*, **67**, 37–69, https://doi.org/10.1007/BF01277501.

Guimond, S. R., G. M. Heymsfield, P. D. Reasor, and A. C. Didlake Jr., 2016: The rapid intensification of Hurricane Karl (2010): New remote sensing observations of convective bursts from the Global Hawk platform. *J. Atmos. Sci.*, **73**, 3617–3639, https://doi.org/10.1175/JAS-D-16-0026.1.

Haase, J. S., B. J. Murphy, P. Muradyan, F. G. Nievinski, K. M. Larson, J. L. Garrison, and K.-N. Wang, 2014: First results from an airborne GPS radio occultation system for atmospheric profiling. *Geophys. Res. Lett.*, **41**, 1759–1765, https://doi.org/10.1002/2013GL058681.

Hajj, G. A., E. R. Kursinski, L. J. Romans, W. I. Bertiger, and S. S. Leroy, 2002: A technical description of atmospheric sounding by GPS occultation. *J. Atmos. Sol.-Terr. Phys.*, **64**, 451–469, https://doi.org/10.1016/S1364-6826(01)00114-6.

Harnisch, F., S. B. Healy, P. Bauer, and S. J. English, 2013: Scaling of GNSS radio occultation impact with observation number using an ensemble of data assimilations. *Mon. Wea. Rev.*, **141**, 4395–4413, https://doi.org/10.1175/MWR-D-13-00098.1.

Healy, S. B., 2011: Refractivity coefficients used in the assimilation of GPS radio occultation measurements. *J. Geophys. Res.*, **116**, D01106, https://doi.org/10.1029/2010JD014013.

——, and J.-N. Thépaut, 2006: Assimilation experiments with CHAMP GPS radio occultation measurements. *Quart. J. Roy. Meteor. Soc.*, **132**, 605–623, https://doi.org/10.1256/qj.04.182.

——, J. Haase, and O. Lesne, 2002: Abel transform inversion of radio occultation measurements made with a receiver inside the earth's atmosphere. *Ann. Geophys.*, **20**, 1253–1256, https://doi.org/10.5194/angeo-20-1253-2002.

——, A. M. Jupp, and C. Marquardt, 2005: Forecast impact experiment with GPS radio occultation measurements. *Geophys. Res. Lett.*, **32**, L03804, https://doi.org/10.1029/2004GL020806.

Hong, S.-Y., Y. Noh, and J. Dudhia, 2006: A new vertical diffusion package with an explicit treatment of entrainment processes. *Mon. Wea. Rev.*, **134**, 2318–2341, https://doi.org/10.1175/MWR3199.1.

Huang, C.-Y., Y.-H. Kuo, S.-H. Chen, and F. Vandenberghe, 2005: Improvements in typhoon forecasts with assimilated GPS occultation refractivity. *Wea. Forecasting*, **20**, 931–953, https://doi.org/10.1175/WAF874.1.

Huang, X.-Y., and Coauthors, 2009: Four-dimensional variational data assimilation for WRF: Formulation and preliminary results. *Mon. Wea. Rev.*, **137**, 299–314, https://doi.org/10.1175/2008MWR2577.1.

Jensen, A. S., M. S. Lohmann, H.-H. Benzon, and A. S. Nielsen, 2003: Full spectrum inversion of radio occultation signals. *Radio Sci.*, **38**, 1040, https://doi.org/10.1029/2002RS002763.

——, ——, A. S. Nielsen, and H.-H. Benzon, 2004: Geometrical optics phase matching of radio occultation signals. *Radio Sci.*, **39**, RS3009, https://doi.org/10.1029/2003RS002899.

Kain, J. S., 2004: The Kain–Fritsch convective parameterization: An update. *J. Appl. Meteor.*, **43**, 170–181, https://doi.org/10.1175/1520-0450(2004)043<0170:TKCPAU>2.0.CO;2.

Kueh, M.-T., C.-Y. Huang, S.-Y. Chen, S.-H. Chen, and C.-J. Wang, 2009: Impact of GPS radio occultation refractivity soundings on a simulation of Typhoon Bilis (2006) upon landfall. *Terr. Atmos. Oceanic Sci.*, **20**, 115–131, https://doi.org/10.3319/TAO.2008.01.21.03(F3C).

Kunii, M., H. Seko, M. Ueno, Y. Shoji, and T. Tsuda, 2012: Impact of assimilation of GPS radio occultation refractivity on the forecast of Typhoon Usagi in 2007. *J. Meteor. Soc. Japan*, **90**, 255–273, https://doi.org/10.2151/jmsj.2012-207.

Kuo, Y.-H., T.-K. Wee, S. Sokolovskiy, C. Rocken, W. Schreiner, D. Hunt, and R. A. Anthes, 2004: Inversion and error estimation of GPS radio occultation data. *J. Meteor. Soc. Japan*, **82**, 507–531, https://doi.org/10.2151/jmsj.2004.507.

Kursinski, E. R., and Coauthors, 1996: Initial results of radio occultation observations of Earth's atmosphere using the global positioning system. *Science*, **271**, 1107–1110, https://doi.org/10.1126/science.271.5252.1107.

——, G. A. Hajj, J. T. Schofield, R. P. Linfield, and K. R. Hardy, 1997: Observing Earth's atmosphere with radio occultation measurements using the Global Positioning System. *J. Geophys. Res.*, **102**, 23 429–23 465, https://doi.org/10.1029/97JD01569.

Leidner, S. M., T. Nehrkorn, J. Henderson, M. Mountain, T. Yunck, and R. N. Hoffman, 2017: A severe weather quick observing system simulation experiment (QuickOSSE) of Global Navigation Satellite System (GNSS) radio occultation (RO) superconstellations. *Mon. Wea. Rev.*, **145**, 637–651, https://doi.org/10.1175/MWR-D-16-0212.1.

Le Marshall, J., and Coauthors, 2012: The application of radio occultation observations for climate monitoring and numerical weather prediction in the Australian region. *Aust. Meteor. Ocean. J.*, **62**, 323–334, https://doi.org/10.22499/2.6204.010.

Li, J., and H. Liu, 2009: Improved hurricane track and intensity forecast using single field-of-view advanced IR sounding measurements. *Geophys. Res. Lett.*, **36**, L11813, https://doi.org/10.1029/2009GL038285.

Liu, H., and J. Li, 2010: An improvement in forecasting rapid intensification of Typhoon Sinlaku (2008) using clear-sky full spatial resolution advanced IR soundings. *J. Appl. Meteor. Climatol.*, **49**, 821–827, https://doi.org/10.1175/2009JAMC2374.1.

——, J. Anderson, and Y.-H. Kuo, 2012: Improved analyses and forecasts of Hurricane Ernesto's genesis using radio occultation data in an ensemble filter assimilation system. *Mon. Wea. Rev.*, **140**, 151–166, https://doi.org/10.1175/MWR-D-11-00024.1.

Liu, Y.-C., S.-H. Chen, and F.-C. Chien, 2011: Impact of MODIS and AIRS total precipitable water on modifying the vertical shear and Hurricane Emily simulations. *J. Geophys. Res.*, **116**, D02126, https://doi.org/10.1029/2010JD014528.

Liu, Z., C. S. Schwartz, C. Snyder, and S.-Y. Ha, 2012: Impact of assimilating AMSU-A radiances on forecasts of 2008 Atlantic tropical cyclones initialized with a limited-area ensemble Kalman filter. *Mon. Wea. Rev.*, **140**, 4017–4034, https://doi.org/10.1175/MWR-D-12-00083.1.

Melhauser, C., and F. Zhang, 2014: Diurnal radiation cycle impact on the pregenesis environment of Hurricane Karl (2010). *J. Atmos. Sci.*, **71**, 1241–1259, https://doi.org/10.1175/JAS-D-13-0116.1.

Mlawer, E. J., S. J. Taubman, P. D. Brown, M. J. Iacono, and S. A. Clough, 1997: Radiative transfer for inhomogeneous atmospheres: RRTM, a validated correlated-k model for the longwave. *J. Geophys. Res.*, **102**, 16 663–16 682, https://doi.org/10.1029/97JD00237.

Montgomery, M. T., and Coauthors, 2012: The PRE-Depression Investigation of Cloud-systems in the Tropics (PREDICT) experiment: Scientific basis, new analysis tools, and some first results. *Bull. Amer. Meteor. Soc.*, **93**, 153–172, https://doi.org/10.1175/BAMS-D-11-00046.1.

Morrison, H., G. Thompson, and V. Tatarskii, 2009: Impact of cloud microphysics on the development of trailing stratiform precipitation in a simulated squall line: Comparison of one- and two-moment schemes. *Mon. Wea. Rev.*, **137**, 991–1007, https://doi.org/10.1175/2008MWR2556.1.

Muradyan, P., J. S. Haase, F. Xie, J. L. Garrison, and J. Voo, 2011: GPS/INS navigation precision and its effect on airborne radio occultation retrieval accuracy. *GPS Solutions*, **15**, 207–218, https://doi.org/10.1007/s10291-010-0183-7.

Murphy, B. J., J. S. Haase, P. Muradyan, J. L. Garrison, and K.-N. Wang, 2015: Airborne GPS radio occultation refractivity profiles observed in tropical storm environments. *J. Geophys. Res. Atmos.*, **120**, 1690–1709, https://doi.org/10.1002/2014JD022931.

Newman, K. M., C. S. Schwartz, Z. Liu, H. Shao, and X.-Y. Huang, 2015: Evaluating forecast impact of assimilating Microwave Humidity Sounder (MHS) radiances with a regional ensemble Kalman filter data assimilation system. *Wea. Forecasting*, **30**, 964–983, https://doi.org/10.1175/WAF-D-14-00091.1.

NOAA/NWS/NCEP/U.S. Department of Commerce, 2004: NCEP ADP global surface observational weather data, October 1999–continuing. Research Data Archive at the National Center for Atmospheric Research, Computational and Information Systems Laboratory, Boulder, CO, accessed 1 March 2016, http://rda.ucar.edu/datasets/ds461.0/.

Parrish, D. F., and J. C. Derber, 1992: The National Meteorological Center's spectral statistical-interpolation analysis system. *Mon. Wea. Rev.*, **120**, 1747–1763, https://doi.org/10.1175/1520-0493(1992)120<1747:TNMCSS>2.0.CO;2.

Poli, P., and J. Joiner, 2004: Effects of horizontal gradients on GPS radio occultation observation operators. I: Ray tracing. *Quart. J. Roy. Meteor. Soc.*, **130**, 2787–2805, https://doi.org/10.1256/qj.03.228.

——, P. Moll, D. Puech, F. Rabier, and S. B. Healy, 2009: Quality control, error analysis, and impact assessment of FORMOSAT-3/COSMIC in numerical weather prediction. *Terr. Atmos. Oceanic Sci.*, **20**, 101–113, https://doi.org/10.3319/TAO.2008.01.21.02(F3C).

Reale, O., W. K. Lau, J. Susskind, E. Brin, E. Liu, L. P. Riishojgaard, M. Fuentes, and R. Rosenberg, 2009: AIRS impact on the analysis and forecast track of Tropical Cyclone Nargis in a global data assimilation and forecasting system. *Geophys. Res. Lett.*, **36**, L06812, https://doi.org/10.1029/2008GL037122.

Rennie, M. P., 2010: The impact of GPS radio occultation assimilation at the Met Office. *Quart. J. Roy. Meteor. Soc.*, **136**, 116–131, https://doi.org/10.1002/qj.521.

Riehl, H., 1954: *Tropical Meteorology*. McGraw-Hill, 392 pp.

Rogers, R., P. Reasor, and S. Lorsolo, 2013: Airborne Doppler observations of the inner-core structural differences between intensifying and steady-state tropical cyclones. *Mon. Wea. Rev.*, **141**, 2970–2991, https://doi.org/10.1175/MWR-D-12-00357.1.

Routray, A., U. C. Mohanty, K. K. Osuri, S. C. Kar, and D. Niyogi, 2016: Impact of satellite radiance data on simulations of Bay of Bengal tropical cyclones using the WRF-3DVAR modeling system. *IEEE Trans. Geosci. Remote Sens.*, **54**, 2285–2303, https://doi.org/10.1109/TGRS.2015.2498971.

Rüeger, J. M., 2002: Refractive index formulae for radio waves. *FIG XXII International Congress*, Washington, DC, 13 pp., https://www.fig.net/resources/proceedings/fig_proceedings/fig_2002/Js28/JS28_rueger.pdf.

Schwartz, C. S., Z. Liu, Y. Chen, and X.-Y. Huang, 2012: Impact of assimilating microwave radiances with a limited-area ensemble data assimilation system on forecasts of Typhoon Morakot. *Wea. Forecasting*, **27**, 424–437, https://doi.org/10.1175/WAF-D-11-00033.1.

——, ——, X.-Y. Huang, Y.-H. Kuo, and C.-T. Fong, 2013: Comparing limited-area 3DVAR and hybrid variational-ensemble data assimilation methods for typhoon track forecasts: Sensitivity to outer loops and vortex relocation. *Mon. Wea. Rev.*, **141**, 4350–4372, https://doi.org/10.1175/MWR-D-13-00028.1.

Skamarock, W. C., and Coauthors, 2008: A description of the Advanced Research WRF version 3. NCAR Tech. Note NCAR/TN-475+STR, 113 pp., https://doi.org/10.5065/D68S4MVH.

Smith, E. K., and S. Weintraub, 1953: The constants in the equation for atmospheric refractive index at radio frequencies. *J. Res. Natl. Bur. Stand.*, **50**, 39–41, https://doi.org/10.6028/jres.050.006.

Sokolovskiy, S., Y.-H. Kuo, and W. Wang, 2005a: Evaluation of a linear phase observation operator with CHAMP radio occultation data and high-resolution regional analysis. *Mon. Wea. Rev.*, **133**, 3053–3059, https://doi.org/10.1175/MWR3006.1.

——, ——, and ——, 2005b: Assessing the accuracy of a linearized observation operator for assimilation of radio occultation data: Case simulations with a high-resolution weather model. *Mon. Wea. Rev.*, **133**, 2200–2212, https://doi.org/10.1175/MWR2948.1.

SSD/OSDPD/NESDIS/NOAA/U.S. Department of Commerce, and NOAA/NWS/NCEP/U.S. Department of Commerce, 2004: NCEP ADP global upper air observational weather data, October 1999–continuing. Research Data Archive at the National Center for Atmospheric Research, Computational and Information Systems Laboratory, Boulder, CO, accessed 1 March 2016, http://rda.ucar.edu/datasets/ds351.0/.

Stewart, S. R., 2011: Tropical cyclone report: Hurricane Karl, 14–18 September 2010. National Hurricane Center Tech. Rep. AL132010, 17 pp., http://www.nhc.noaa.gov/data/tcr/AL132010_Karl.pdf.

Syndergaard, S., E. R. Kursinski, B. M. Herman, E. M. Lane, and D. E. Flittner, 2005: A refractive index mapping operator for assimilation of occultation data. *Mon. Wea. Rev.*, **133**, 2650–2668, https://doi.org/10.1175/MWR3001.1.

Torn, R. D., and D. Cook, 2013: The role of vortex and environment errors in genesis forecasts of Hurricanes Danielle and Karl (2010). *Mon. Wea. Rev.*, **141**, 232–251, https://doi.org/10.1175/MWR-D-12-00086.1.

Wang, K.-N., J. L. Garrison, U. Acikoz, J. S. Haase, B. J. Murphy, P. Muradyan, and T. Lulich, 2016: Open-loop tracking of rising and setting GPS radio-occultation signals from an airborne platform: Signal model and error analysis. *IEEE Trans. Geosci. Remote Sens.*, **54**, 3967–3984, https://doi.org/10.1109/TGRS.2016.2532346.

——, ——, J. S. Haase, and B. J. Murphy, 2017: Improvements to GPS airborne radio occultation in the lower troposphere through implementation of the phase matching method. *J. Geophys. Res. Atmos.*, **122**, 10 266–10 281, https://doi.org/10.1002/2017JD026568.

Wang, X., 2011: Application of the WRF hybrid ETKF–3DVAR data assimilation system for hurricane track forecasts. *Wea. Forecasting*, **26**, 868–884, https://doi.org/10.1175/WAF-D-10-05058.1.

Ware, R., and Coauthors, 1996: GPS sounding of the atmosphere from low Earth orbit: Preliminary results. *Bull. Amer. Meteor. Soc.*, **77**, 19–40, https://doi.org/10.1175/1520-0477(1996)077<0019:GSOTAF>2.0.CO;2.

Weissmann, M., and Coauthors, 2011: The influence of assimilating dropsonde data on typhoon track and midlatitude forecasts. *Mon. Wea. Rev.*, **139**, 908–920, https://doi.org/10.1175/2010MWR3377.1.

Weng, Y., and F. Zhang, 2012: Assimilating airborne Doppler radar observations with an ensemble Kalman filter for convection-permitting hurricane initialization and prediction: Katrina (2005). *Mon. Wea. Rev.*, **140**, 841–859, https://doi.org/10.1175/2011MWR3602.1.

Willoughby, H. E., 2012: Distributions and trends of death and destruction from hurricanes in the United States, 1900–2008. *Nat. Hazards Rev.*, **13**, 57–64, https://doi.org/10.1061/(ASCE)NH.1527-6996.0000046.

——, E. N. Rappaport, and F. D. Marks, 2007: Hurricane forecasting: The state of the art. *Nat. Hazards Rev.*, **8**, 45–49, https://doi.org/10.1061/(ASCE)1527-6988(2007)8:3(45).

Xie, F., J. S. Haase, and S. Syndergaard, 2008: Profiling the atmosphere using the airborne GPS radio occultation technique: A sensitivity study. *IEEE Trans. Geosci. Remote Sens.*, **46**, 3424–3435, https://doi.org/10.1109/TGRS.2008.2004713.

Yunck, T. P., G. F. Lindal, and C.-H. Liu, 1988: The role of GPS in precise Earth observation. *Proc. Position Location and Navigation Symp.: Navigation into the 21st Century,* Orlando, FL, IEEE, 251-258, https://doi.org/10.1109/PLANS.1988.195491.

Zhang, F., and Y. Weng, 2015: Predicting hurricane intensity and associated hazards: A five-year real-time forecast experiment with assimilation of airborne Doppler radar observations. *Bull. Amer. Meteor. Soc.*, **96**, 25–33, https://doi.org/10.1175/BAMS-D-13-00231.1.

Zou, X., H. Liu, R. A. Anthes, H. Shao, J. C. Chang, and Y.-J. Zhu, 2004: Impact of CHAMP radio occultation observations on global analysis and forecasts in the absence of AMSU radiance data. *J. Meteor. Soc. Japan*, **82**, 533–549, https://doi.org/10.2151/jmsj.2004.533.